Moho Depth of Northern Baja California, Mexico, From Teleseismic Receiver Functions

E. E. Ramírez[1], Klaus Bataille[2], J. A. Vidal-Villegas[3], J. M. Stock[4], J. Ramírez-Hernández[1].

[1]Instituto de Ingeniería, Universidad Autónoma de Baja California (UABC). Calle de la normal S/N, Insurgentes Este 21280, Mexicali, Baja California, México.

[2]Departamento de Ciencias de la Tierra, Universidad de Concepción, Chile (UdeC). Cabina 13, Casilla 160-C, Concepción Región del Bíobio, Chile.

[3]Departamento de Sismología, División Ciencias de la Tierra, Centro de Investigación Científica y de Educación Superior de Ensenada, México (CICESE). Carretera Ensenada-Tijuana 3918, Zona Playitas 22860 Ensenada, Baja California, México.

[4]Seismological Laboratory, Division of Geological and Planetary Sciences, California Institute of Technology (Caltech). Pasadena, California 91125 U.S.A.

Corresponding author: Erik Ramírez (ramirez.erik@uabc.edu.mx)

Key Points:

- Receiver Function
- Moho Northern Baja California, Mexico
- Mexicali Valley
- Peninsular Ranges of Baja California
- Moho

Abstract

We estimated Moho depth from data recorded by permanent and temporary broadband seismic stations deployed in northern Baja California, Mexico using the receiver function technique. This region is composed, mainly, of two subregions of contrasting geological and topographical characteristics: The Peninsular Ranges of Baja California (PRBC), a batholith with high elevations (up to 2600 m above mean sea level); and the Mexicali Valley (MV) region, a sedimentary environment at around the mean sea level. Crustal thickness derived from the *P*-to-*S* converted phases at 29 seismic stations were analyzed in 3 profiles: two that cross the two subregions, in a ~W-E direction, and the third one that runs over the PRBC in a N-S direction. For the PRBC region, Moho depths vary from 35 to 45 km, from 33ºN to 32ºN; and from 30 to 46 km depth from 32ºN to 30.5ºN. From a profile that crosses the subregions in the W-E direction; Moho depths vary from 45 to ~34 km under the PRBC; with an abrupt change of depth under the Main Gulf Escarpment, from ~32 to 30 km; and depths of 17-20 km under the MV region. Moho depths of the profile that runs, of an almost W-E direction at ~31.5º N, follow the eltimetry from 0 to 2600 m: from ~30 to 40 km; and became shallower (16 km depth) as the profile reaches the Gulf of California. These results show that deeper Moho is related to higher elevations with an abrupt change under the Main Gulf Escarpment.

1 Introduction

The relative motion between the Pacific and North American plates in the northern Baja California (nBC), Mexico, region is dominated by a transtension regime that generates normal and strike-slip faults (Stock et al., 1991). This plate boundary generates significant earthquakes

in nBC that have reached magnitudes of 7.2 (the 2010 El Mayor-Cucapah earthquake). This significant seismicity is recorded by the Southern California Seismic Network, in the USA side of the border, and by the Northwest Mexico Seismic Network (RESNOM; CICESE, 1980), in the nBC region.

Northern Baja California is composed, mainly, by two contrasting geological subregions divided by the Main Gulf Escarpment (MGE; Fig 1): the sedimentary environment of the Mexicali Valley subregion (MV) and the granitic environment of the Peninsular Ranges of Baja California (PRBC). The PRBC is a Mesozoic batholith composed of two belts separated by a magnetite-ilmenite boundary (Gastil et al., 1991): the western batholith with more mafic composition, ages from 140 to 105 Ma, and elevations from 0 to ~900 meters above mean sea level (m.a.m.s.l); and the eastern batholith, formed between 105 and 80 Ma, characterized by more silicic intrusions and metasedimentary rocks, with elevations from ~900 to 1980 m.a.m.s.l at the Sierra Juárez mountain range (around 32ºN) and up to 3095 m.a.m.s.l at the San Pedro Mártir mountain range (~ 31ºN). Active faults within the PRBC include the strike-slip San Miguel-Vallecitos fault system (e.g., Hirabayashi et al., 1996), the strike-slip Tres Hermanos fault system (e.g., Frez et al., 2000) and the strike-slip Agua Blanca fault (e.g., Wetmore et al., 2019). Faults at the eastern boundary of the PRBC include the San Pedro Mártir fault, which has Holocene scarps but does not currently have significant seismicity (Cid-Villegas et al., 2017).

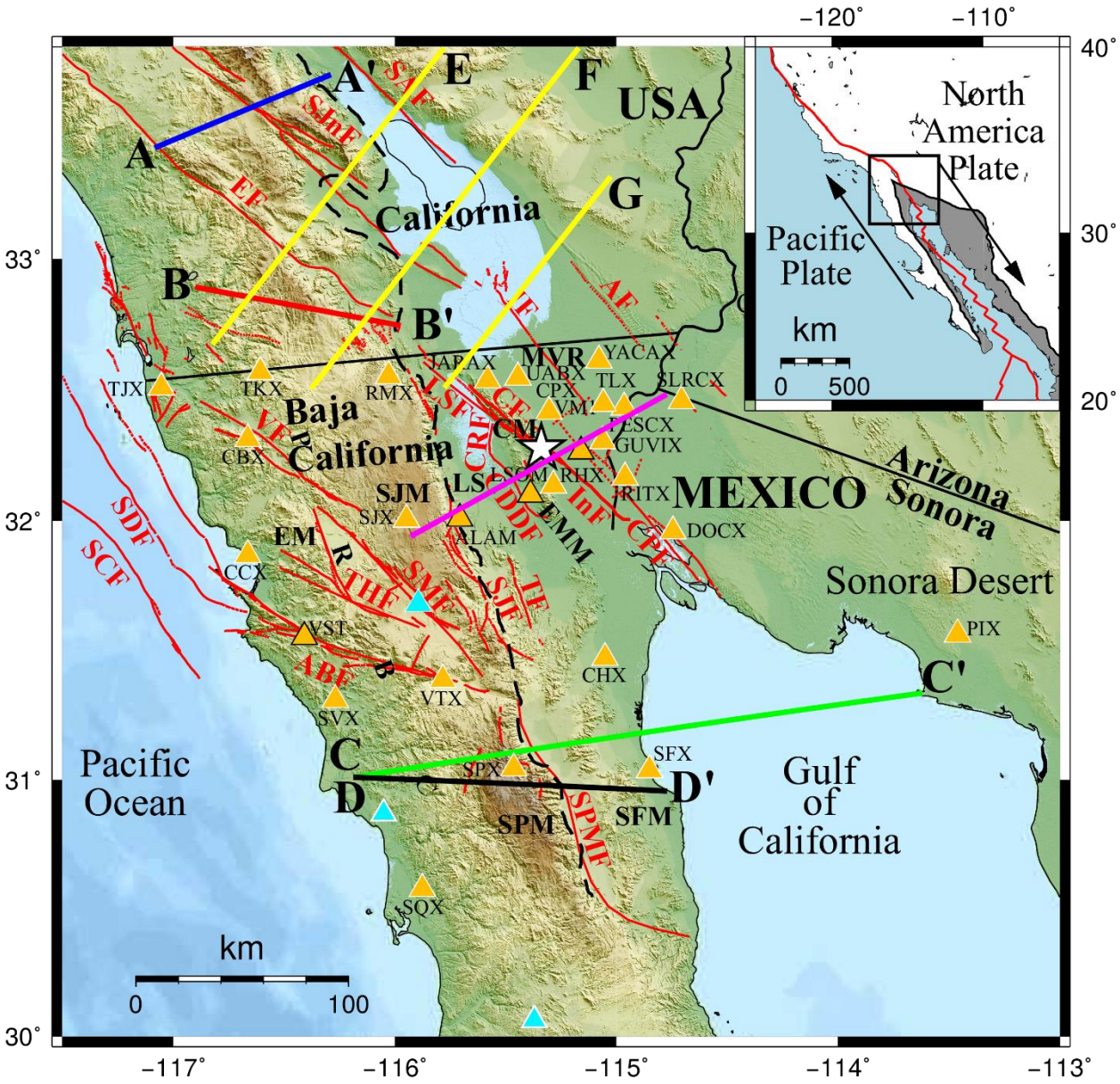

Figure 1. Map of the northern Baja California region. The interaction between North America and the Pacific plates is shown with the arrows; the grey area shows the Gulf Extensional Province (Suárez-Vidal et al., 2008). The northern Baja California (Mexico) and southern California (USA) map show the main faults (grey lines) and the broadband seismic stations used in this study: orange triangles (Table 1). Cyan triangles are the stations used by Persaud *et al.* (2007) from the NARS-Baja Project (Clayton *et al.*, 2014). The black lines indicate the profiles used in previous receiver function studies: A-A' (Lewis *et al.*, 2000); B-B' (Ichinose *et al.*, 1996); C-C' (Lewis *et al.*, 2001); D-D' (Reyes *et al.*, 2001); profiles E-G (Ozakin and Ben-Zion, 2015). The dashed black line represents the MGE that divides the Peninsular Ranges of Baja

California and the Mexicali Valley regions (PRBC and VMR, respectively). White star indicates the epicenter of the 4 april 2010 El Mayor-Cucapah earthquake. Abbreviations: CM, Cucapah Mountains; EMM, El Mayor Mountains; LS, Laguna Salada; SFM, San Felipe Mountains; SJM, Sierra Juárez Mountains; SPM, San Pedro Mártir Mountains. Faults abbreviations: ABF, Agua Blanca fault; AF, Algodones fault; CDDF, Cañada David Detachment fault; CF, Cucapah fault; CPF, Cerro Prieto fault; CRF, Cañón Rojo fault; EF, Elsinore fault; IF, Imperial fault; InF, Indiviso fault; LSF, Laguna Salada fault; SDF, San Diego fault; SAFZ; San Andreas fault; SCF, San Clemente fault; SJF, Sierra Juárez fault; SJnF, San Jacinto fault; SMF, San Miguel fault; TF, Tinajas fault; THF, Tres Hermanos fault; VF, Vallecitos fault.

The MV region, the northwestern part of the Gulf Extensional Province (Suárez-Vidal et al., 2008; inset Fig. 1), is composed principally of two basins divided by the Cucapah and El Mayor mountain ranges: the Mexicali Valley and the Laguna Salada basins (Fig. 1). The Laguna Salada Basin is a tectonic depression 20 km wide by 100 km long (García-Abdeslem et al., 2001), and is delimited by the MGE to the west and by the Cucapah and El Mayor mountain ranges to the east. The sedimentation of this basin began when the Cucapah and El Mayor mountain ranges uplifted during the Pleistocene (Martín-Barajas et al., 2001). The Mexicali Valley Basin has 5-6 km depth, and was filled by Neogene sediments transported by the Colorado River (Pelayo et al., 1991). This basin is located east of the Cucapah and El Mayor mountain ranges. Within the MV region is the Cerro Prieto Basin, a pull-apart basin that connects the Cerro Prieto and Imperial faults (Suárez-Vidal et al., 2008, González et al., 2001); this regional tectonic feature is the Cerro Prieto Spreading Center. There is also the fault system comprising the Laguna Salada-Cucapah-Indiviso faults, the last one a previously unknown fault that ruptured during the 4 april 2010 M_W 7.2 El Mayor-Cucapah Earthquake (Gonzalez-Ortega et al., 2014). We analyzed the earthquakes in nBC in the time interval 2000 to 2020 (from the

97 RESNOM catalog), by accounting the epicenters inside a polygon that surrounds the above-
98 mentioned faults, and estimate that these two fault systems generate ~50% of the seismicity in
99 nBC.

100 Under this complex tectonic environment, receiver function studies have been carried out
101 to provide a better understanding of the crustal thickness and its relationship with the surface
102 elevation and the extensional processes of the region (Lewis et al., 2001). North of the U.S.A.-
103 Mexico border (southernmost California), in the Mesozoic Peninsular Ranges batholith, Ichinose
104 et al. (1996) and Lewis et al. (2000) performed receiver function studies at latitudes ~33.5ºN and
105 33ºN, respectively (Fig. 1). Moho depths proposed by these two authors are similar: 37-36 km at
106 the western part of the batholith to 25-27 km depth at the eastern side of the batholith. Persaud et
107 al. (2007) used receiver functions (RFs) to determine the Moho depth at 17 stations south of 34
108 ºN in Southern California, reporting depths from 38 to 25 km. More recently Ozakin and Ben-
109 Zion (2015) analyzed receiver functions at a series of broadband seismometers in southern
110 California in the area from 32.5ºN to 34.75ºN (profiles E-G, Fig. 1) and reported Moho depth
111 ranges from 35-40 km (beneath part of the Peninsular Ranges) to 10 km (beneath the Salton
112 Sea).

113 At present, the only two efforts to estimate the Moho depth in nBC were those done by
114 Lewis et al. (2001) and Reyes et al. (2001) that used *P*-to-*S* converted phases from teleseismic
115 records and *Pg-Pn* travel times, from regional events, respectively (Fig. 1). These studies used
116 seismic stations from the North Baja Transect installed during 1997 and 1998 at latitude ~31ºN
117 (Astiz et al., 1998). The profile used by Lewis et al. (2001) starts at the Pacific coast, crosses the
118 PRBC, and ends at the Gulf of California coast of Sonora, Mexico, using a station in the Gulf of
119 California itself, while Reyes et al. (2001) used only data from stations in the Peninsular Ranges.

Their results for the Moho are similar for the PRBC section, depths of: 31-33 km near the Pacific coast; 40-42 km beneath the western part of the PRBC; and 19-20 km toward the Gulf of California. These studies have been carried out using profiles that cross the PRBC approximately in a west-east direction with seismic stations installed over granitic environments. Note that Persaud et al. (2007) obtained a Moho depth for three additional sites in the northern PRBC, NE71, NE72 and NE73 (cyan triangles of Fig. 1), as part of a regional study using RFs from NARS-Baja seismometers surrounding the Gulf of California (Clayton et al., 2004).

The seismically active region of nBC between ~32 ºN and 33ºN has a gap of receiver function studies, leaving this latitudes section with no Moho depth estimation for the PRBC nor, most importantly, for the sedimentary environment of the MV region. To perform a receiver function study in nBC, we used stations belonging to RESNOM (Fig. 1) that were updated from short-period to three-component broadband seismic stations as a consequence of the occurrence of the 4 april 2010 M_W 7.2 El Mayor-Cucapah earthquake (Vidal-Villegas et al., 2018). To have better coverage in a profile, in an SW-NE direction (that crosses the PRBC, the MGE, and the MV), we installed temporary broadband stations (Fig. and Table 1). Receiver functions from both permanent and temporary stations were calculated using the *P*-to-*S* converted phases from teleseismic earthquakes and then modeled to obtain a Moho depth at each station. Estimating the Moho depth of nBC will provide parameters to characterize the crustal structure related to the PRBC and the MV regions and the tectonic evolution, especially for the MV where the Cerro Prieto Spreading Center is located, as part of the San Andreas-Gulf of California rift system.

2 Data

2.1 Instrumentation.

To estimate the Moho depth in nBC, we used 29 broadband seismic stations. These 29 stations comprised 24 permanent RESNOM stations and five temporary stations (Fig. and Table 1). The instrumentation of the permanent seismic stations, at present, includes: two stations with Güralp CMG-40Twith Reftek 71A-07 recorder, and CMG-40TD with Reftek 130 recorder (flat response from 30 s and 120 s to 50 Hz, respectively); nine stations equipped with Güralp CMG-3ESPC and Reftek 130 (120 s to 50 Hz); 13 stations instrumented with Nanometrics Trillium Compact (NTC) with Reftek 130 (120 s to 50 Hz). The temporary seismic stations were instrumented as follows: four stations with NTC with Nanometrics Taurus (120 s to 50 Hz); one station equipped with Geotech KS-2000 with Reftek 130 (120 s to 50 Hz).

Table 1. Permanent (RESNOM) and temporary broadband stations in northern Baja California.

Station Code	Sensor	Latitude (º)	Longitude (º)
ALAM[a,b]	NTC-120s	32.0085	-115.7074
CBX	CMG-40T	32.3131	-116.6636
CCX	CMG-3ESPC	31.8678	–116.6645
CHX	CMG-40T / CMG-3ESPC	31.4721	–115.0521
CPX	CMG-3ESPC	32.4195	–115.3050
DOCX	NTC-120s	31.9594	–114.7451
GUVIX	NTC-120s	32.3029	–115.0762
JARAX	NTC-120s	32.5378	–115.5815
LSOM[a]	NTC-120s	32.1000	-115.3878
PESCX	NTC-120s	32.4338	–114.9649
PIX	CMG-3ESPC	31.5629	–113.4599

RHX	CMG-3ESPC / NTC-120s	32.135	–115.2843
RITX	NTC-120s	32.1659	–114.9613
RMX	CMG-3ESPC / NTC-120s	32.5535	–116.0290
SFX	CMG-3ESPC	31.0376	–114.8510
SJX	CMG-3ESPC	32.0048	–115.9480
SLRCX	NTC-120s	32.4579	–114.7058
SPX	CMG-3ESPC	31.0451	–115.4660
SQX	CMG-3ESPC	30.5762	–115.8758
SVX	NTC-120s	31.3271	-116.2510
TJX	CMG-3ESPC / NTC-120s	32.5102	–117.0543
TKX	CMG-3ESPC / NTC-120s	32.5687	–116.6075
TLX	CMG-40TD	32.448	-115.109
UABX	CMG-3ESPC / NTC-120s	32.6316	-115.4447
VM1[a,b]	NTC-120s	32.2653	-115.1596
VST[a]	NTC-120s	31.5528	-116.4085
VTX	CMG-3ESPC	31.3914	-115.7840
YACAX	NTC-120s	32.6054	-115.0938

[a]Temporary broadband station.

[b]Temporary broadband station that later became a permanent seismic station of the RESNOM.

Ramirez et al. (2019) described the installation facilities of permanent broadband stations. Temporary stations were powered by 4 deep-cycle batteries (interchangeable every 3 months) and had the following shelters: for stations ALAM, OJSN, and VM1, a concrete base with metal lid was constructed; station VST used a former accelerometer station shelter; station LSOM was buried and covered with plastic boxes under sand over wood. Temporary stations operated differently: ALAM, 3 years; OJSN, 3 years; VM1, 3 years; VST, 1 year; LSOM, 3 moths.

164

165 2.2 Teleseismic earthquakes**.**

166 A preliminary earthquake selection, performed searching in the USGS Earthquake
167 Catalog (see Data and Resources) for $M \geq 6.5$ earthquakes (from 1 January 2014, to 1 July 2016),
168 resulted in 133 earthquakes. In order to select only earthquakes between distances of 30 and 95º
169 from the central point of the array at 32.1ºN, 115.7ºW, a Matlab script (see Data and Resources)
170 was written. After this process, 90 teleseismic earthquakes were selected.

171 **S**eismograms from permanent stations, of all 90 teleseismic earthquakes, were requested
172 from RESNOM (see Data and Resources). From each temporary station's database, the 90
173 teleseismic earthquakes were searched and extracted.

174 After merging records from permanent and temporary seismic stations, we performed two
175 steps of quality control: i) checking that the seismic signal was good: presence of three-
176 component seismic signal and not electronic noise due to the absence of seismic signal; ii)
177 selecting only the events where the *P*-arrival was clear enough above the ambient noise. The
178 seismic ambient noise is high in stations located in the MV region than in the PRBC (Ramírez et
179 al., 2019, Fig. 2 shows this issue). After these steps, 66 teleseismic earthquakes were selected for
180 the receiver function computation (Table 2).

181

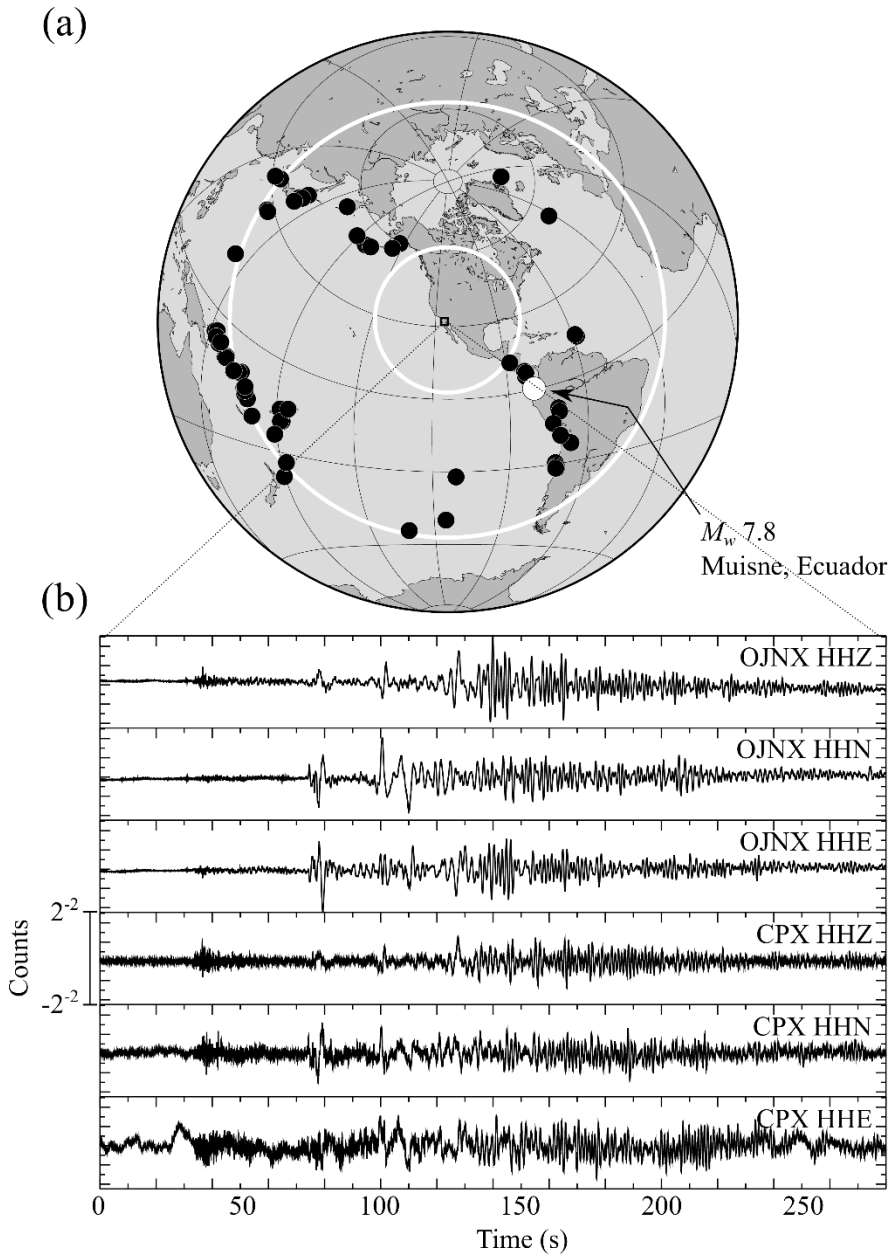

Figure 2. Teleseismic earthquakes used in this study. (a) Global distribution of the earthquakes used (circles filled in black and white). White circles indicate the 30 and 95º distances from the center of the study area (black rectangle). The white filled circle indicates the position of the 16 April 2016 Muisne, Ecuador earthquake M_w 7.8. (b) Three-component records of this earthquake of stations OJNX and CPX, located in the PRBC and the MVR, respectively.

Table 2. Earthquakes used for the receiver function analysis[a,b].

Date	Origin Time (HH:MM:SS)	Latitude (°)	Longitude (°)	Depth (km)	Magnitude (M_w)	Distance (°)	Azimuth (°)	Back-Azimuth (°)
28 April 2016	19:33:24.07	-16.0429	167.3786	24.00	7.0	87.94	236.82	56.82
16 April 2016	23:58:36.98	0.3819	-79.9218	20.59	7.8	46.35	133.32	313.32
15 April 2016	16:25:06.22	32.7906	130.7543	10.00	7.0	89.77	270.34	90.34
03 April 2016	08:23:52.32	-14.3235	166.8551	26.00	6.9	87.39	237.94	57.94
30 January 2016	03:25:12.22	53.9776	158.5463	177.00	7.2	62.12	289.45	109.45
24 January 2016	10:30:30.23	59.6363	-153.4051	129.00	7.1	37.04	317.12	137.12
14 January 2016	03:25:33.64	41.9723	142.7810	46.00	6.7	76.68	276.88	96.88
26 November 2015	05:45:18.40	-9.1825	-71.2574	602.75	6.7	59.22	134.28	314.28
24 November 2015	22:45:38.88	-10.5372	-70.9437	606.21	7.6	60.42	134.98	314.98
18 November 2015	18:31:04.57	-8.8994	158.4217	12.59	6.8	91.33	243.41	63.41
13 November 2015	20:51:31.03	31.0009	128.8729	12.00	6.7	92.14	269.29	89.29
11 November 2015	02:46:19.83	-29.5097	-72.0585	10.00	6.9	74.30	146.14	326.14
09 November 2015	16:03:46.07	51.6394	-173.0746	15.00	6.5	45.51	294.72	114.72
07 November 2015	07:31:43.87	-30.8796	-71.4519	46.00	6.8	75.71	146.42	326.42
20 October 2015	21:52:02.56	-14.8595	167.3028	135.00	7.1	87.33	237.49	57.49
21 September 2015	17:40:00.06	-31.7275	-71.3792	35.00	6.6	76.42	146.76	326.76
16 September 2015	22:54:32.86	-31.5729	-71.6744	22.44	8.3	76.14	146.87	326.87
12 August 2015	18:49:24.08	-9.3293	157.8772	6.43	6.5	92.01	243.33	63.33
10 August 2015	04:12:15.81	-9.3438	158.0525	22.00	6.6	91.87	243.27	63.27
27 July 2015	04:49:46.40	52.3760	-169.4458	29.00	6.9	43.33	297.18	117.18
18 July 2015	02:27:33.82	-10.4012	165.1409	11.00	7.0	86.59	240.66	60.66
16 July 2015	15:16:33.78	13.8672	-58.5479	20.00	6.5	54.98	109.36	289.36
10 July 2015	04:12:42.54	-9.3070	158.4030	12.00	6.7	91.56	243.20	63.20
3 June 2015	12:18:30.27	27.7375	139.7254	460.00	6.5	86.61	267.17	87.17
30 June 2015	11:23:02.11	27.8386	140.4931	664.00	7.8	86.00	267.21	87.21
29 June 2015	07:00:09.00	56.5940	-156.4300	72.60	6.7	37.08	310.56	130.56
22 June 2015	21:45:19.48	-11.0559	163.6959	11.19	6.9	88.13	240.74	60.74
20 June 2015	22:48:53.42	-10.8759	164.1694	11.00	6.8	87.65	240.69	60.69
19 June 2015	15:25:21.08	-54.3312	-132.1618	7.20	6.7	87.72	189.47	9.47
12 June 2015	21:12:58.89	38.9056	142.0317	35.00	6.8	78.79	274.60	94.60
07 June 2015	07:10:19.59	-7.2175	154.5567	10.00	7.1	93.67	245.30	65.30
05 June 2015	01:44:06.38	-5.4624	151.8751	55.00	7.5	95.00	246.85	66.85
01 June 2015	08:06:03.48	-5.2005	151.7773	44.00	6.8	94.94	247.01	67.01
17 June 2015	15:52:51.48	-15.8815	-178.6005	10.00	6.5	77.05	231.45	51.45
29 March 2015	23:48:31.01	-4.7294	152.5623	41.00	7.5	94.03	247.08	67.08
16 February 2015	23:06:28.27	39.8558	142.8808	23.00	6.7	77.73	275.32	95.32
13 February 2015	18:59:12.23	52.6487	-31.9016	16.68	7.1	61.33	71.47	251.47
11 February 2015	18:57:22.46	-23.1125	-66.6880	223.00	6.7	72.45	139.75	319.75

23 January 2015	03:47:27.05	-17.0309	168.5200	219.96	6.8	87.60	235.89	55.89
07 January 2015	05:07:07.51	5.9045	-82.6576	8.00	6.5	40.48	130.48	310.48
08 December 2014	08:54:52.52	7.9401	-82.6865	20.00	6.6	39.04	128.38	308.38
07 December 2014	01:22:02.18	-6.5108	154.4603	23.00	6.6	93.37	245.70	65.70
16 November 2014	22:33:20.45	-37.6478	179.6621	22.00	6.7	92.25	220.87	40.87
01 November 2014	18:57:22.38	-19.6903	-177.7587	434.00	7.1	78.88	228.91	48.91
14 October 2014	03:51:34.46	12.5262	-88.1225	40.00	7.3	32.00	127.92	307.92
09 October 2014	02:14:31.44	-32.1082	-110.8112	16.54	7.0	64.49	175.93	355.93
17 September 2014	06:14:45.41	13.7641	144.4294	130.00	6.7	90.84	258.59	78.59
20 August 2014	23:21:45.52	-14.5980	-73.5714	101.00	6.8	61.75	139.25	319.25
21 July 2014	14:54:41.00	-19.8015	-178.4001	615.42	6.9	79.41	229.14	49.14
11 July 2014	19:22:00.82	37.0052	142.4525	20.00	6.5	79.53	273.27	93.27
04 July 2014	15:00:27.86	-6.2304	152.8075	20.00	6.5	94.62	246.23	66.23
29 June 2014	17:15:09.34	-14.9831	-175.5096	18.00	6.7	74.19	230.57	50.57
23 June 2014	20:53:09.70	51.8486	178.7352	109.00	7.9	50.58	292.20	112.20
13 May 2014	06:35:24.24	7.2096	-82.3045	10.00	6.5	39.82	128.83	308.83
12 May 2014	18:38:36.70	-49.9403	-114.7995	10.47	6.5	82.17	179.47	359.47
04 May 2014	09:15:52.88	-24.6108	179.0856	527.00	6.6	84.28	227.66	47.66
01 May 2014	06:36:35.55	-21.4542	170.3546	106.00	6.6	88.74	232.86	52.86
13 April 2014	12:36:19.23	-11.4633	162.0511	39.00	7.4	89.71	241.01	61.01
12 April 2014	20:14:39.30	-11.2701	162.1481	22.56	7.6	89.52	241.08	61.08
11 April 2014	07:07:23.13	-6.5858	155.0485	60.53	7.1	92.92	245.51	65.51
01 April 2014	23:46:47.26	-19.6097	-70.7691	25.00	8.2	67.31	140.31	320.31
18 February 2014	09:27:13.12	14.6682	-58.9272	14.83	6.5	54.26	108.74	288.74
07 February 2014	08:40:13.55	-15.0691	167.3721	122.00	6.5	87.40	237.35	57.35
02 February 2014	09:26:37.82	-32.9076	-177.8806	44.26	6.5	87.64	222.07	42.07
01 January 2014	16:03:29.00	-13.8633	167.2490	187.00	6.5	86.81	238.06	58.06
30 August 2012	13:43:25.17	71.4410	-10.6050	14.00	6.8	64.18	56.42	236.42

[a]Origin time, location and magnitude provided by USGS (see Data and Resources).

[b] Distance, Azimuth and Back-Azimuth, resulted from Matlab-based scripts, with computations relative to the central point of the array: 32.1ºN, 115.7ºW.

3 Methodology

3.1 Data Preprocessing.

196 Moho estimation was performed using the 66 earthquakes selected (Fig. 2 and Table 2).
197 In order to compute the RFs of each broadband seismic station in nBC, we first preprocessed the
198 records as follows: 1) Order each merged teleseismic mseed file in one separated folder named
199 “Event_YYYY_MM_DD_hh_mm_ss”, following the structure used for data gathering using the
200 Standing Order for Data (Owens et al., 2004); 2) Manually select and extract the seismic signal 2
201 minutes before and 3 minutes after the first *P*-wave arrival using SeisAn (Havskov and
202 Ottemöller, 1999); 3) Convert each trace of the seismograph into a SAC file (Goldstein and
203 Snoke, 2005; see Data and Resources); 4) Collect the SEED Dataless from the permanent
204 seismic stations (see Data and Resources) and generate them for the temporary seismic stations
205 (poles and zeros, and normalization constants); 5) Remove the instrument response of the
206 seismographs using ObsPy (Beyreuther et al., 2010; see Data and Resources) under Spyder (The
207 Scientific Python Development Environment; see Data and Resources), using a band-pass filter
208 from 0.05-0.1 to 10-20 Hz for stations in the PRBC and from 0.05-0.1 to 10-15 Hz for stations in
209 the MV region; 6) Write to the SAC file-header the station information (latitude, longitude, and
210 elevation) using SAC macros; 7) With a series of Spyder scripts, we changed/updated the
211 following variables of each SAC file-header: *cmpinc*, 90 to the horizontal components, and 0 to
212 the vertical one; *cmpaz*, 90 to the E-W component, and 0 to the N-S and vertical component; 8)
213 We write to each SAC file-header, using Spyder scripts, the corresponding teleseismic
214 information into the SAC variables: event depth, *evdp*; event latitude and longitude, *evla*, and
215 *evlo*, respectively; event origin time, *o*, referring to the start time of the file, *starttime*; 9) Add the
216 theoretical first *P*-wave arrival to the SAC files of each teleseismic earthquake using TauP (see
217 Data and Resources).

218

3.2 Receiver Function Computations.

Receiver functions were computed using rf module for Python (see Data and Resources). The preprocessed data is rotated to the great circle path with the angles given by the back-azimuth and inclination values of the traces. After this, the signal was bandpass filtered from 0.4 to 1 Hz. Then, the frequency domain deconvolution, L component is deconvolved from the other components, was calculated to remove possible anisotropy, lateral heterogeneity beneath the station, and propagation effects.

The deconvolution was performed by computing the Toeplitz auto-correlation matrix of the source (Wang et al., 2016), then inverting it, adding noise, and multiplying with the cross-correlation vector of response and source (Arushanian et al., 1983). To increase the signal-noise ratio, we stacked, for each station, all the RFs computed from the teleseismic earthquakes available for such station. For this analysis, we only interpreted the radial RFs.

3.3 Depth computations.

To estimate the Moho depth, we converted *Ps-P* times by using the Matlab toolbox FuncLab (Eagar and Fouch, 2012; Porritt and Miller, 2018). This estimation was obtained using two methods: the FuncLab-implemented Common Conversion Point (CCP), and *H-κ* stacking (both described in Eagar et al., 2011; Eagar and Fouch, 2012). The CCP is a back-projection method where the amplitudes of each receiver function are placed in the respective ray path of the teleseismic earthquake. In this stacking, where the signal is enhanced, the amplitudes and depths are connected based on the position of the ray piercing point. Then the IASP91 (Kennett and Engdahl, 1991) 1-D velocity model is used to compute the 1-D ray tracing and the time-to-

241 depth conversion. The *H-κ* stacking is a technique used to determine average crustal properties
242 based on RFs (Zhu and Kanamori, 2000). This method considers a homogeneous, horizontal, and
243 isotropic layer (crust) over a half-space (upper mantle). With the *H-κ* stacking, the Moho depth
244 (H), the *P* to *S*-wave velocity ratio (*Vp/Vs* of *κ*), and the Poisson's ratio are estimated by
245 measuring the *Ps-P* time from the RFs.

246

247 **4 Results**

248 4.1 Receiver Functions of nBC.

249 The RFs were computed from 66 earthquakes, with good azimuthal coverage, especially
250 along the Peru-Chile Trench; in the Tonga-Hikurangi Trench, from the Solomon Sea to New
251 Zealand; and in the Aleutian Trench, from the Gulf of Alaska to Japan (Fig. 2 and right panel of
252 Fig. 3).

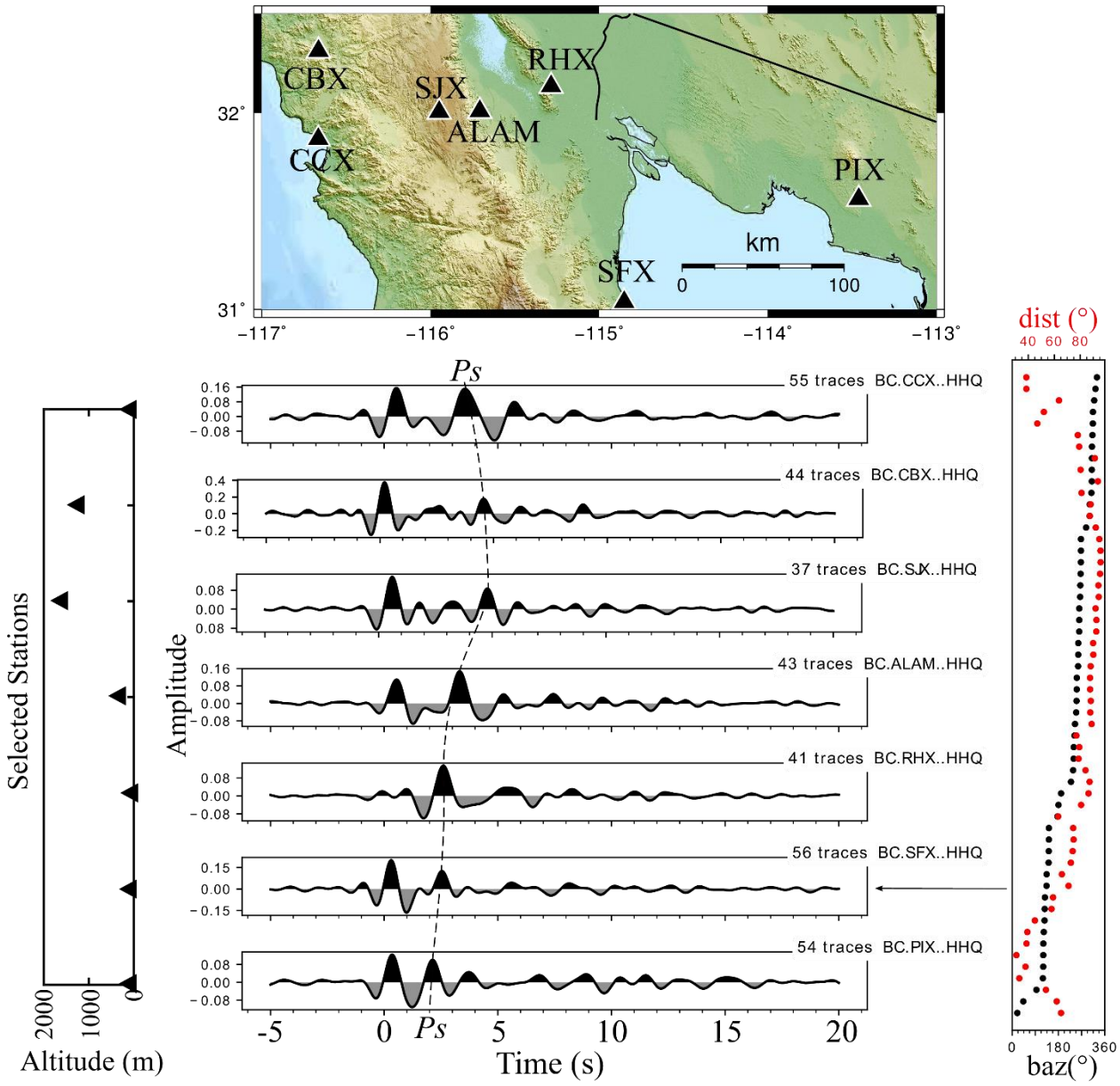

Figure 3. Map of the selected stations of nBC and the Sonora Desert (top panel). The stacked RFs of the selected stations are shown in the central plots, from station CCX to PIX, from top to bottom, in a west to east direction. The legend at the top-right of each stacked receiver function plot indicates the number of earthquakes used, the network code (BC), the station code, and the component code (HHQ). The dashed black line indicates the interpreted *Ps* arrivals. The right panel is a double plot that shows, for example, the back-azimuth coverage (black dots), and the distance of the earthquakes from the central point of the array (grey dots). The left panel is a plot of the altitude of the corresponding selected stations.

The stacked RFs of the PRBC show the Ps conversion around 4.1 s. As examples, we selected stations CCX, CBX, and SJX, located at the Pacific Coast, around central PRBC, and at the eastern side of the PRBC (top of the MGE), respectively. For the MV region, we identified the Ps conversions around 2.0 s. The selected stations for showing their stacked RFs are ALAM, RHX, SFX, and PIX, located at the eastern base of the PRBG (at the bottom of the MGE, inside Laguna Salada), in the Mexicali Basin (east of El Mayor Mountain), at the Gulf of California coast, and in the Sonoran Desert (now in the North American Plate), respectively.

4.2 Back-Projection Receiver Functions.

The back-projection results of the RFs were selected from three profiles (Fig. 4.a): A1-A1', from the PRBC, crossing the MGE into the MV; A2-A2', which crosses the BC peninsula, around San Pedro Mártir mountain, and ends at the Sonora desert; A3-A3', an almost N-S profile that runs through the PRBC. The A1-A1' profile (upper panel of Fig 4.b) presents positive RFs with high amplitudes (RFs Amplitudes of ~1) at depths of around 30 km, for stations close to the Pacific coast of the peninsula (CCX, VST, and CBX); from 30 to 42 km for stations located around the Sierra Juárez mountains (VTX and SJX); 25-30 km for stations located in the transition segment between the PRBC and MV (ALAM and RMX); 17-25 km for stations located in the MV region (JARAX – SLRX). The back-projected amplitudes of the A3-A3' profile present positive high values (RFs Amplitudes of ~1) at the following depths (upper panel of Fig. 4.c): 35-42 km for stations south 31ºN (SPX and SQX); 32-46 km for stations located between 31º and 32º N (VTX, SVX, VTS, and SJX, ; except for stations ALAM and CCX located at the east and west limits of the PRBC, respectively, at around sea level); and 35-40 km

285 for stations between 32ºN and 33ºN (CBX, RMX, TKX, and TJX). The amplitudes of the back-
286 projected RFs of the A2-A2' (upper panel of Fig. 4.d) profile present high positive values at
287 depths of ~35 km for stations located near the Pacific coast (VST and SVT); 35-40 km for
288 stations around the San Pedro Mártir mountains (VTX and SPX); ~23 km for stations near the
289 Gulf of California coast (CHX and SFX); and ~20 km for the station located in the Sonoran
290 Desert (PIX).

291

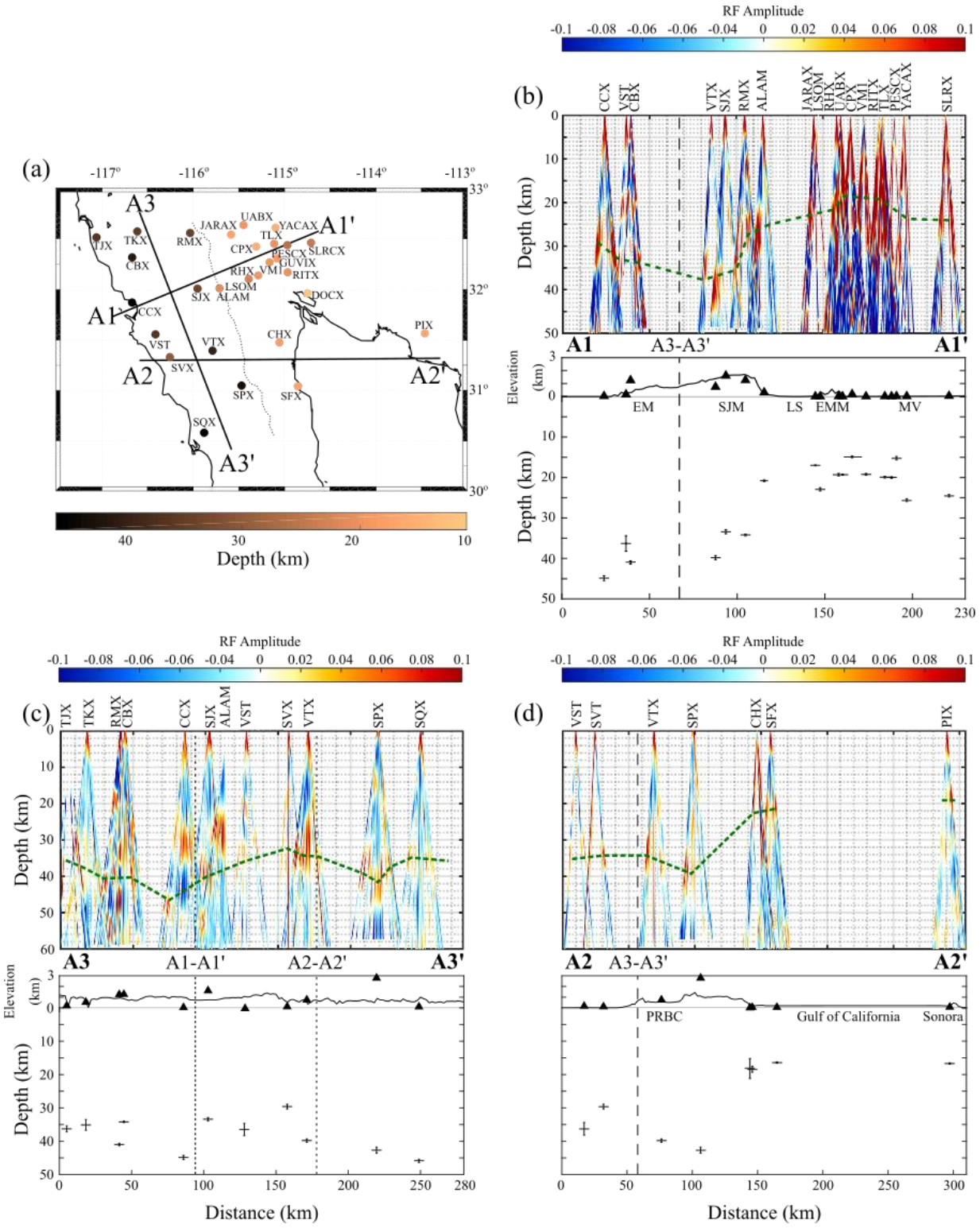

Figure 4. (a) Map of estimated depths from the *H-κ* analysis at each seismic station. Black thick lines indicate the analyzed profiles. The thin dotted line indicates the MGE. Plots (b), (c), and (d)

show the back-projected RFs of the profiles A1-A1', A2-A2', and A3-A3', respectively; the dashed green line indicates the suggested Moho from the interpreted ray paths. The figure from bellow of (b), (c), and (d) of the A1-A1', A2-A2', and A2-A2', respectively, shows: the results of Moho depth estimation with error bars from the *H-κ* procedure (Table 3); the elevation of the center of each profile, black line; mean sea level, thin black line; location of each station alongside the profile, black triangles; the location at which the A3-A3' crosses the profile, dashed line; the location at which A1-A1' and A2-A2' cross the profile, dotted lines.

4.3 *H-κ* computations.

The results of computations of the *H-κ* are shown in Table 3 and Fig. 4 (divided into the three profiles). From depth results shown in Table 3, we estimate a Moho depth of ~38 km, for stations deployed in the PRBC, and ~19 km, for stations located in the MV region. Like in the back-projection analysis, results of Moho depth from the *H-κ* computation (Table 3) are analyzed in the same A-A' profiles. Stations projected into the A1-A1' profile (lower panel of Fig. 4.b) show that Moho depths under stations located on the Pacific coast of the Peninsula (CCX, VST, and CBX) vary from 35-45 km. Moho depths of stations deployed in the Sierra Juárez mountains region (VTX, SJX, and RMX) range from 35-40 km. The Moho depths of stations in the MV region range from 15-25 km. The A3-A3' profile (lower panel of Fig. 4c) has the following Moho depths: from ~35 km dipping to a maximum of 45 km, in the north-south direction, for profile section from 33ºN to 32ºN; from ~32 km dipping into 46 km depth, in the north-south direction, for the profile section between latitudes 32ºN and ~30.5ºN. The profile A2-A2' (lower panel of Fig. 4d) presents Moho depths of (Table 3): ~30 and 36 km for stations near the Pacific coast (SVT and VST); 40-42 km for stations at the center of the Peninsula (VTX and SPX); 16-19 km for stations near the Gulf of California (SFX and CHX); and ~17 km for the station located in Sonora, Mexico (PIX).

320

321 **Table 3.** Receiver function results and Moho estimations of each station.

Station code	Elevation (m)	*Ps-P* time (s)	*H* (km)	V_P/V_S, κ	Poisson's Ratio
ALAM	315	3.2	20.8 ± 0.2	1.84 ± 0.02	0.292 ± 0.005
CBX	1250	4.5	41.0 ± 0.4	1.96 ± 0.01	0.324 ± 0.004
CCX	33	3.6	44.9 ± 0.6	1.97 ± 0.02	0.327 ± 0.004
CHX	49	2.5	18.4 ± 0.9	1.74 ± 0.06	0.252 ± 0.024
CPX	179	3.2	14.9 ± 0.2	1.95 ± 0.02	0.321 ± 0.005
DOCX	13	1.4	10.9 ± 0.2	1.95 ± 0.03	0.208 ± 0.015
GUVIX	14	3.3	18.2 ± 3.0	1.87 ± 0.10	0.299 ± 0.026
JARAX	5	2.5	17.0 ± 0.1	1.85 ± 0.01	0.292 ± 0.004
LSOM	5		22.9 ± 0.4	1.55 ± 0.02	0.140 ± 0.012
PESCX	23	1.8	25.6 ± 0.3	1.72 ± 0.01	0.246 ± 0.005
PIX	72	2.2	16.7 ± 0.2	1.81 ± 0.02	0.280 ± 0.005
RHX	16	2.5	19.3 ± 0.3	1.75 ± 0.02	0.260 ± 0.008
RITX	14	1.8	20.0 ± 0.2	1.54 ± 0.01	0.137 ± 0.008
RMX	1265	4.7	34.2 ± 0.2	1.61 ± 0.01	0.186 ± 0.005
SFX	48	2.6	16.4 ± 0.2	1.97 ± 0.02	0.327 ± 0.004
SJX	1609	4.8	33.4 ± 0.5	1.57 ± 0.01	0.158 ± 0.008
SLRCX	49	1.2	24.5 ± 0.3	1.75 ± 0.02	0.256 ± 0.008
SPX	2790	4.9	42.7 ± 0.9	2.04 ± 0.03	0.341 ± 0.006
SQX	101	3.4	45.9 ± 0.5	1.96 ± 0.01	0.323 ± 0.003
SVX	111	4.1	29.6 ± 0.7	1.82 ± 0.03	0.282 ± 0.010
TJX	198	3.9	36.3 ± 0.9	1.62 ± 0.02	0.194 ± 0.012
TKX	535	3.3	35.1 ± 1.6	1.90 ± 0.04	0.309 ± 0.011
TLX	17	2.0	19.9 ± 0.2	1.95 ± 0.02	0.321 ± 0.004
UABX	5	3.5	19.3 ± 0.1	1.49 ± 0.01	0.090 ± 0.001
VM1	10	2.2	19.2 ± 0.2	1.64 ± 0.02	0.204 ± 0.009
VST	163	3.7	36.3 ± 1.9	1.65 ± 0.04	0.209 ± 0.0.21
VTX	746	4.1	39.8 ± 0.5	1.92 ± 0.02	0.315 ± 0.005

YACAX	21	1.9	15.2 ± 0.4	2.06 ± 0.04	0.346 ± 0.008

Moho depths from previous studies (Ichinose et al., 1996; Lewis et al. 2000, 2001; Ozakin et al. 2015; Persaud et al., 2007; Ramírez-Ramos et al., 2015) were extracted of digitized to compare those with results from our *H*-κ computations. To analyze the results from different authors, we interpolated, with the triangulation-based natural method, all Moho estimations in the region of study. The interpretation of Moho in northern Baja California, alongside the topography, is shown in two 3-D plots of Fig 5.

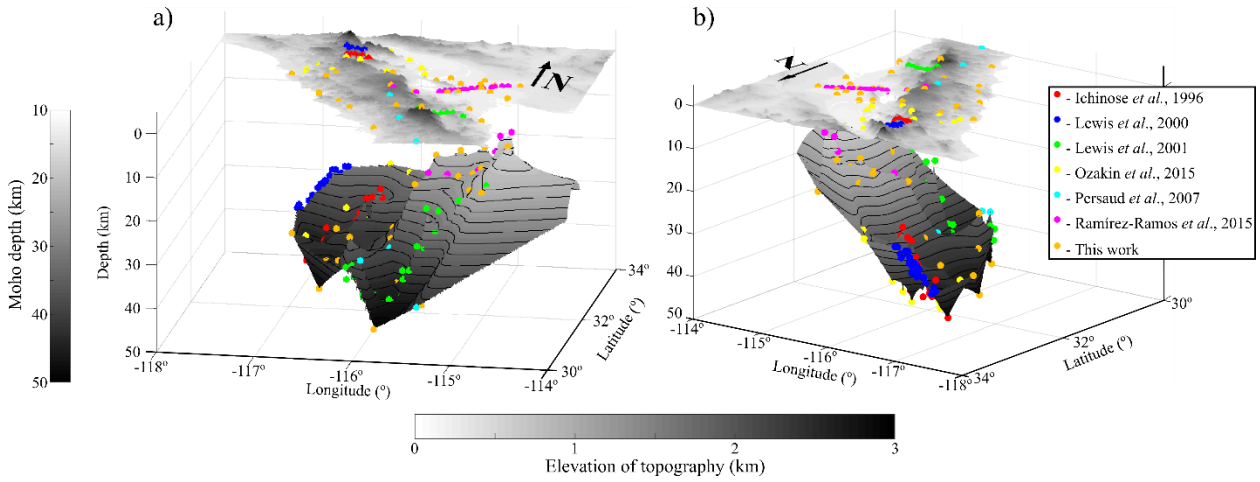

Figure 5. Unified Moho model for northern Baja California. Each figure's upper plot is the local altimetry, and the color dots indicate the stations used for each study (right-handed legend box). The lower plots of (a) and (b) are the triangulation-based natural neighbor interpolation Moho estimations by seismic studies in northern Baja California; color dots represent the Moho estimations of each regional studies indicated in the right-handed legend box. Left and lower handed color bars indicate Moho depth and elevation (both in km), respectively. (a) Elevations and Moho estimations of northern Baja California from an S-N view. (b) Elevations and Moho estimations in northern Baja California from an NW-SE perspective.

340

341 **5 Analysis**

342 Results from the back-projection of the RFs are similar to those resulting from the *H-κ*
343 computations (Fig 4.b-d). We base the following analysis on the Moho depths resulting from the
344 *H-κ* computations since they are more compressed in space (depth) throughout the profile (due to
345 the variable incidence angles of the RF ray).

346 From the results of the A1-A1' profile (Fig. 4.a-b), we see that the Moho depths become
347 shallower, starting at 45 km depth at the western part of the profile, reaching ~34 km depth
348 below stations near the top of the MGE, following the high elevations of the Sierra Juárez
349 mountain range but not for the Pacific coast where elevations decrease to sea level. The Moho
350 depth changes abruptly when the profile enters into the MV region: from ~32 km below the
351 PRBC to a 20 km depth at the lower part of the MGE (at Laguna Salada basin). Note that the
352 location of this abrupt change is most tightly constrained in map view between stations RMX
353 and ALMX (Fig. 4.a), at or slightly west of the Main Gulf Escarpment. The Moho depths for the
354 MV region section of the A1-A1' profile are shallow, and stable at ~20 km depth. Comparing the
355 Moho depths of the MV with those reported by Ramírez-Ramos et al. (2015), in a refraction
356 profile (using *Pn* arrivals) that ran in the same position A1-A1', we get similar results. For the
357 Laguna Salada basin, we get ~20 km Moho depth, while the authors reported 19 km depth.
358 Moreover, for the MV basin, we get ~17 km Moho depth, while they reported 15 km.

359 The almost N-S profile (A3-A3') runs entirely through the PRBC, a stable topographic
360 region: elevations start at sea level at the Pacific coast, and reach 2600 m above sea level at the
361 top of the MGE. Nevertheless, Moho depths show some variations in a N-S direction: from 33º

to 32º N, the Moho deepens from 35 km to 45 km; from 32ºN to 30.5ºN the Moho deepens from ~30 km to 46 km. The mean Moho depth for the PRBC (~38 km) is close to the 42 km reported by Nava and Brune (1982). This model consists of a flat-layer model for the PRBC derived from a refraction profile that ran almost in the same position as A3-A3'. The Moho depth in the PRBC, at 31.7ºN, determined to be 33.7 km (Persaud et al., 2007), consistent with the results we find here.

The Moho depths for the A2-A2' profile follow the elevation profile (lower panel of Fig 4.c). From west to east, the Moho deepens as elevation reaches its maximum (2600 m above mean sea level; station SPX): from ~30 km to 42 km depth. Continuing along the E direction, we observe that by decreasing elevation, when going into the Gulf of California, the Moho goes from 42 km to 16 km depth, almost the same as the depth below PIX located in the Sonoran Desert. The Moho depths reported by Lewis et al. (2001) from the receiver function profile (Fig. 1) present the same behavior and values as those from the A2-A2' profile, 55 km south of C-C' profile (Lewis et al., 2001; Fig. 1).

Our results can be compared to the RF results from southernmost California, reported by Ozakin and Ben-Zion (2015) even though our data are from northwestern Mexico, just south of the SW end of their profiles E, F, and G (Fig. 1). Ozakin and Ben-Zion (2015) noted that the depth to the Moho varied along strike in a complex fashion, which is also characteristic of our results. For example, on our profile A3-A3', along the axis of the Peninsular Ranges, the Moho depths vary generally in the range from 35 to 45 km but without any systematic direction of gradient. The Moho depths > 40 km are beneath the Peninsular Ranges in two locations 150 km apart at latitudes between 30.5ºN and 32ºN. In combination with the Moho depths reaching 40

384 km reported by Ozakin and Ben-Zion at 34ºN beneath the batholith, this suggests a N-S variation
385 in Moho depth under the batholith, with a wavelength of 150 to 200 km.

386 We only identify one station (DOCX, Table 3) with Moho depth nearly as shallow as the
387 10 km depths reported by Ozakin and Ben-Zion beneath the Salton Sea. This station is in
388 Sonora, just E of the southern extension of the Cerro Prieto Fault, where it enters the northern
389 Gulf of California (Fig. 1) and its Moho depth by *H-k* analysis is 10.9 +/- 0.2 km. The other
390 Moho depths in the MV in our study area are in the range of 15-20 km.

391 Figures 5a and 5b are 3D views of the integrated Moho structure from the northern
392 Peninsular Ranges, California to the southern PRBC and Salton Trough Province (STP), from all
393 seismic exploring studies performed in the region (Ichinose et al., 1996; Lewis et al. 2000, 2001;
394 Ozakin et al. 2015; Persaud et al., 2007; Ramírez-Ramos et al., 2015; and this study). Figure 5a
395 is a view from South to North direction (STP is on the right, and PRBC is on the left), and Figure
396 5b is a view from North to South direction (now PRBC is on the right, and STP is on the left).
397 From both figures, it is clear that the Moho depth in STP is shallower than in PRBC. There is a
398 correlation between the topography in the PRBC region and Moho depth variation: high
399 elevations correspond to deep values, given support to the Airy's theory. Regarding the STP,
400 where Mexicali Valley is comprised, the figures show a depth of Moho of around 17 km with no
401 marked variations (smooth Moho).

402 **6 Conclusions**

403 In a profile that crosses the PRBC and the MV region, Moho depths became shallower
404 from west to east: 45 to ~34 km under the PRBC to the 17 km under the MV region; with an
405 abrupt change in depth under the MGE, from ~32 km to 20 km depth in a west to east direction.

Moreover, under the MV region, we propose a near-constant Moho depth of 17-20 km. The profile that runs almost N-S though the PRBC, with stable topography, Moho depths vary from 35 to 45 km, from 33ºN and 32ºN; and from 30 to 46 km depth from 32ºN to 30.5ºN. The Moho depths, of an almost west to the east direction (at ~31.3ºN), follow the altitude of the topography from 0 to 2600 m above mean sea level: from ~30 to 40 km.

The Moho becomes shallower as the profile reaches the Gulf of California coast to a 16 km depth in both the Peninsula of Baja California and in the station located on the coast of Sonora. Our results are similar to previous studies done north and south of the study region (Lewis et al., 2001; Ozakin and Ben-Zion, 2015; Persaud et al., 2007), and with refraction studies done in profiles that ran close to the ones here reported (Nava and Brune, 1982; Ramírez-Ramos et al., 2015). The results of our study show that, in general, the Moho depth follows the elevations of the stations, deeper for stations with high altitudes and shallower for stations near the sea level, with an abrupt change in depth at the surrounding area of the Main Gulf Escarpment. Moho depths of stations on the MV region are shallow, suggesting an extension of the lower crust of the pull-apart basin that connects the Cerro Prieto and Imperial faults (Cerro Prieto Spreading Center), within the regional section of the rifting system San Andreas-Gulf of California.

Acknowledgments

Part of the financial support for this project was provided by CONACYT (CB-2009-133019 SEP-CONACYT). The first author worked under the Scholarship Number 254218 granted by the National Council of Science and Technology of Mexico (CONACYT), the CONACYT 2018 Foreign Mobility Fellowship (291250), and by the Mobility Fellowship granted by the Autonomous University of Baja California: research residence (announcement

76). Alejandra Núñez-Leal facilitated teleseismic data streams from the local seismic network (RESNOM). For the installation and service for the seismic stations, the authors acknowledge Oscar Gálvez, Luis Orozco, and Ignacio Méndez, from the Earth Sciences Division of CICESE. Sergio Arregui provided the main script used for creating the maps in Generic Mapping Tools.

Data Resources

Raw and processed seismic signals, as well as the poles and zeros of stations and main scripts used can be found in https://zenodo.org/record/4017974#.X1Z_SHkzaUl (dor: 10.5281/zenodo.4017974). Teleseismic catalog was obtained from the USGS Earthquake Catalog, available at https://earthquake.usgs.gov/earthquakes/search/ (last accessed September 2020). Some computations were made writing Matlab scripts, available at https://www.mathworks.com/products/matlab.html (last accessed September 2020). Data from the Northwest Mexico Seismic Network are available, since 10 September 2014, from the Incorporated Research Institutions for Seismology Data Management Center (IRIS-DMC) at http://ds.iris.edu/mda/BC (last accessed September 2020). The teleseismic data used in this study and the stations Dataless are available upon request to M. Alejandra Nuñez-Leal. (anunez@cicese.mx).Preprocessing scripts (macros) were written in Seismic Analysis Code (SAC), available at http://ds.iris.edu/ds/nodes/dmc/software/downloads/sac/ (last September 2020). ObsPy is available at https://github.com/obspy/obspy/wiki (last accessed July 2019). Spyder is available at https://www.spyder-ide.org/ (last accessed September 2020). The rf Python framework for receiver function computations is available at https://rf.readthedocs.io/en/latest/ (last accessed July 2019). The *P*-wave travel times were computed, and added to earthquakes data with TauP, available at http://www.seis.sc.edu/TauP/ (last accessed September 2020). The

452 FuncLab toolbox used for estimating the Moho depth is available at
453 https://robporritt.wordpress.com/software/ (last accessed September 2020). Some plots were
454 made using the Generic Mapping Tools v.5.3.1 available at http://gmt.soest.hawaii.edu/ (last
455 accessed September 2020).
456

457 **References**

458 Arushanian, O. B., Samarin, M. K., Voevodin, V. V., Tyrtyshnikov, E. E., Garbow, B. S., Boyle,
459 J. M., Cowell, W. R., & Dritz, K. W. (1983). TOEPLITZ package users' guide. Technical Report
460 ANL-83-16, *Moskovskij Gosudarstvennyj University*, Argonne National Laboratory, CM-
461 P00069203.
462
463 Astiz, L., Castro, R., Eakins, J., Vernon, F. L., Rebollar, C., Day, S. M., & Brune, J. N. (1998).
464 The North Baja Transect (NBT): A seismic experiment in our backyard, paper presented at 10th
465 Annual IRIS Workshop, Santa Cruz, Calif., 1998.
466
467 Beyreuther, M., Barsch, R., Krischer, L., Megies, T., Behr, Y., & Wassermann, J. (2010). ObsPy:
468 A Python Toolbox for Seismology. *Seismoogical. Research Letters, 81(3)*, 530-533, doi:
469 10.1785/gssrl.81.3.530.
470
471 Centro de Investigación Científica y de Educación Superior de Ensenada (CICESE), Ensenada
472 Baja California, México (1980): Red Sísmica del Noroeste de México, doi: 10.7914/SN/BC.
473
474 Cid-Villegas, G., Mendoza, C., & Ferrari, L. (2017). Mexico Quaternary Fault Database. *Terra*
475 *Digitalis, 1(1)*, 1-9, doi: 10.22201/igg.terradigitalis.2017.1.3.50.
476
477 Clayton, R. W., Trampert, J., Rebollar, C., Ritsema, J., Persaud, P., Paulssen, H., Pérez-Campos,
478 X., van Wettum, A., Pérez-Verti, A., & DiLuccio, F. (2004). The NARS-Baja seismic array in
479 the Gulf of California rift zone. *Margins Newsletter, **13***, 1-4.

Goldstein, P., & Snoke, A. (2005). "SAC Availability for the IRIS Community", Incorporated Institutions for Seismology Data Management Center Electronic Newsletter.

Eagar, K. C., Fouch, M. J., James, D. E., & Carlson, R. W. (2011). Crustal structure beneath the High Lava Plains of eastern Oregon and surrounding regions from receiver function analysis. *Journal of Geophysical Research: Solid Earth, 116 (B2)*, doi: 10.1029/2010JB007795.

Eagar, K. C., & Fouch, M. J. (2012). FuncLab: A MATLAB interactive toolbox for handling receiver function datasets. *Seismological Research Letters, 83(3),* 596-603, doi: 10.1785/gssrl.83.3.596.

Frez, J., González, J. J., Acosta, J. G., Nava, F. A., Méndez, I., Carlos, J., García-Arthur, R. E., & Alvarez, M. (2000). A detailed microseismicity study and current stress regime in the Peninsular Ranges of northern Baja California, Mexico: The Ojos Negros region. *Bulletin of the Seismological Society of Amearica, 90(5),* pp.1133-1142, doi: 10.1785/0119990164.

García-Abdeslem, J., Espinoza-Cardeña, J. M., Munguía, L., Wong, V. M., & Ramírez-Hernández, J. (2001). Crustal structure from 2-D gravity and magnetic data modeling, magnetic power spectrum inversion, and seismotectonics in the Laguna Salada basin, northern Baja California, Mexico. *Geofisica Internacional, 40 (2),* 67–85.

Gastil, R. G., Kimbrough, J., Tainosho, Y., Shimizu, M., & Gunn, S. (1991). Plutons of the eastern Peninsular Ranges, southern California, USA and Baja California, Mexico. In Geological Excursions in Southern California and México: San Diego, California, *Geological Society of America Annual Meeting Guidebook*, 319-331.

González, M., Munguía, L., Vidal, A., Wong, V., González, M., & Suárez, F. (2001). Two M_w 4.8 Cerro Prieto, Baja California, México, Earthquakes on 1 June and 10 September 1999: Strong-Motion Observations. *Bulletin of the Seismological Society of America, 91(6),* 1456-1470, doi: 10.1785/0120000033.

Gonzalez-Ortega, A., Fialko, Y., Sandwell, D., Nava-Pichardo, A. F., Fletcher, J., Gonzalez-Garcia, J., & Funning, G. (2014). El Mayor–Cucapah (Mw 7.2) earthquake: Early near-field postseismic deformation from InSAR and GPS observations. *Journal of Geophysical Research, 119(2),* 1482–1497, doi: 10.1002/2013JB010193.

Havskov, J., & Ottemöller, L. (1999). SeisAn earthquake analysis software. *Seismological Research Lettets, 70(5),* 532–534, doi: 10.1785/gssrl.70.5.532.

Hirabayashi, C.K., Rockwell, T.K., Wesnousky, S.G., Stirling, M.W., & Suarez-Vidal, F. (1996). A neotectonic study of the San Miguel-Vallecitos fault, Baja California, Mexico. *Bulletin of the Seismological Society of America, 86(6),* pp.1770-1783.

Ichinose, G., Day, S., Magistrale, H., Prush, T., Vernon, F., & Edelman, A. (1996). Crustal thickness variations beneath the Peninsular Ranges, southern California. *Geophysical Research Letters, 23(22),* 3095–3098, doi: 10.1029/96GL03020.

Kennett, B. L. N., & Engdahl, E.R. (1991). Traveltimes for global earthquake location and phase identification. *Geophysical Journal International, 105(2),* 429-465, doi: 10.1111/j.1365-246X.1991.tb06724.x.

Lewis, J. L., Day, S. M., Magistrale, H., Eakins, J., & Vernon, F. (2000). Regional crustal thickness variations of the Peninsular Ranges, southern California. *Geology, 28(4),* 303-306, doi: 10.1130/0091-7613(2000)28<303:RCTVOT>2.0.CO;2.

Lewis, J. L., Day, S. M., Magistrale, H., Castro, R. R., Rebollar, C., Astiz, L., Eakins, J., Vernon, F. L., & Brune, J. N. (2001). Crustal thickness of the peninsular ranges and gulf extensional province in the Californias. *Journal of Geophysical Research: Solid Earth, 106(B7),* 13599-13611, doi: 10.1029/2001JB000178.

Martín-Barajas, A., Vázquez-Hernández, S., Carreño, A. L., Helenes, J., Suárez-Vidal, F., & Alvarado-Rosales, J. (2001). Late Neogene stratigraphy and tectonic control on facies evolution in the Laguna Salada basin, northern Baja California, Mexico. *Sedimentary Geology*, *144*, 5–35, doi: 10.1016/S0037-0738(01)00133-6.

Nava, F. A., & Brune, J. N. (1982). An earthquake-explosion reversed refraction line in the Peninsular Ranges of southern California and Baja California Norte. *Bulletin of the Seismological Society of America, 72(4),* 1195–1206.

Owens, T. J., Crotwell, H. P., Groves, C., & Oliver-Paul, P. (2004). SOD: Standing order for data, *Seismological Research Letters, 75(4),* 515-520, doi: 10.1785/gssrl.75.4.515-a.

Ozakin, Y., & Ben-Zion, Y. (2015). Systematic receiver function analysis of the Moho geometry in the Southern California plate-boundary region. *Pure and Applied Geophysics, 172(5),* 1167-1184, doi: 10.1007/s00024-014-0924-6.

Pelayo, A., Razo, L. A., Gutiérrez, N. L. C. A., Arellano, G. F., Espinoza, J. M., & Quijano, J. L. (1991). Main geothermal fields of Mexico: Cerro Prieto geothermal field, Baja California, Geological Society of America, *The Geology of North America*, *Vol. P-3, Economic Geology, México*, 23–58.

Persaud P., Pérez-Campos, X., & Clayton, R. (2007). Crustal thickness variations in the margins of the Gulf of California from receiver functions. *Geophysical Journal International, 170(2),* 687–699, https://doi.org/10.1111/j.1365-246X.2007.03412.x.

Porritt, R. W., & Miller, M. S. (2018). Updates to FuncLab, a Matlab based GUI for handling reveiver functions. *Computers and Geosciences, 111*, 260-271, doi: 10.1016/j.cageo.2017.11.022.

570 Ramírez-Ramos, E. E., Vidal-Villegas, A., González-Fernández, A., & Stock, J. (2015). A
571 crustal velocity model for the southern Mexicali Valley, Baja California, Mexico. *Seismological*
572 *Research Letters, 86(1),* 181–191, doi: 10.1785/0220140007.
573
574 Ramirez, Erik E., Vidal-Villegas, J. A., Nuñez-Leal, M. A., Ramírez-Hernández, J., Mejía-Trejo,
575 A., & Rosas-Verdugo, E. (2019). Seismic Noise Levels in Northern Baja California, Mexico.
576 *Bulletin of the Seismological Society of America, 109(2),* 610-620, doi: 10.1785/0120180155.
577
578 Reyes, L. M., Rebollar, C. J., & Castro, R. (2001). Depth of the Moho in northern Baja
579 California using (P_g-P_n) travel times. *Geofísica Internacional, 40(1),* 1-9.
580
581 Stock, J. M., Martín-Barajas, A., Suárez-Vidal, F., & Miller, M. M. (1991). Miocene to Holocene
582 extensional tectonics and volcanic stratigraphy of NE Baja California, Mexico, in Geological
583 Excursions in Southern California and Mexico: Guide Book, *1991 Annual Meeting, Geological*
584 *Society of America*, San Diego, California, 21–24 October, 44–67.
585
586 Suárez-Vidal, F., Mendoza-Borunda, R., Nafarrete-Zamarripa, L. M., Ramírez, J., & Glowacka,
587 E. (2008). Shape and dimensions of the Cerro Prieto pull-apart basin, Mexicali, Baja California,
588 Mexico, based on the regional seismic record and surface structures. *International Geology*
589 *Review, 50(7),* 636–649, doi: 10.2747/0020-6814.50.7.636.
590
591 Vidal-Villegas, J. A., Munguía, L., González-Ortega, J. A., Nuñez-Leal, M. A., Ramírez, E.,
592 Mendoza, L., Castro, R. R., & Wong, V. (2018). The Northwest Mexico Seismic Network: Real-
593 time seismic monitoring in northern Baja California and northwestern Sonora, Mexico.
594 *Seismological Research Letters, 89(2A),* 324-337, doi: 10.1785/0220170183.
595
596 Wang, L., Zhao, Q., Gao, J., Xu, Z., Fehler, M., & Jiang, X. (2016). Seismic sparse-spike
597 deconvolution via Toeplitz-sparse matrix factorization. *Geophysics, 81(3),* V169-V182, doi:
598 10.1190/geo2015-0151.1.
599

Wetmore, P. H., Malservisi, R., Fletcher, J. M., Alsleben, H., Wilson, J., Callihan, S., Springer, A., González-Yajimovich, O., & Gold, P. O. (2019). Slip history and the role of the Agua Blanca fault in the tectonics of the North American–Pacific plate boundary of southern California, USA and Baja California, Mexico. *Geosphere, 15(1)*, 119-145, doi: 10.1130/GES01670.1.

Zhu, L., & Kanamori, H. (2000). Moho depth variation in southern California from teleseismic receiver functions. *Journal of Geophysical Research: Solid Earth, 105(B2)*, 2969-2980, doi: 10.1029/1999JB900322.

Figure Captions

Figure 1. Map of the northern Baja California region. The interaction between North America and the Pacific plates is shown with the arrows; the grey area shows the Gulf Extensional Province (Suárez-Vidal et al., 2008). The northern Baja California (Mexico) and southern California (USA) map show the main faults (grey lines) and the broadband seismic stations used in this study: orange triangles (Table 1). Cyan triangles are the stations used by Persaud et al. (2007) from the NARS-Baja Project (Clayton et al., 2014). The black lines indicate the profiles used in previous receiver function studies: A-A' (Lewis et al., 2000); B-B' (Ichinose et al., 1996); C-C' (Lewis et al., 2001); D-D' (Reyes et al., 2001); profiles E-G (Ozakin and Ben-Zion, 2015). The dashed black line represents the MGE that divides the Peninsular Ranges of Baja California and the Mexicali Valley regions (PRBC and VMR, respectively). White star indicates the epicenter of the 4 april 2010 El Mayor-Cucapah earthquake. Abbreviations: CM, Cucapah Mountains; EMM, El Mayor Mountains; LS, Laguna Salada; SFM, San Felipe Mountains; SJM, Sierra Juárez Mountains; SPM, San Pedro Mártir Mountains. Faults abbreviations: ABF, Agua Blanca fault; AF, Algodones fault; CDDF, Cañada David Detachment fault; CF, Cucapah fault;

CPF, Cerro Prieto fault; CRF, Cañón Rojo fault; EF, Elsinore fault; IF, Imperial fault; InF, Indiviso fault; LSF, Laguna Salada fault; SDF, San Diego fault; SAFZ; San Andreas fault; SCF, San Clemente fault; SJF, Sierra Juárez fault; SJnF, San Jacinto fault; SMF, San Miguel fault; TF, Tinajas fault; THF, Tres Hermanos fault; VF, Vallecitos fault.

Figure 2. Teleseismic earthquakes used in this study. (a) Global distribution of the earthquakes used (dots filled in black and white). White circles indicate the 30º and 95º distances from the center of the study area (black rectangle). The white filled circle indicates the position of the 16 April 2016 Muisne, Ecuador earthquake M_w 7.8. (b) Three-component records of this earthquake of stations OJNX and CPX, located in the PRBC and the MVR, respectively.

Figure 3. Map of the selected stations of nBC and the Sonora Desert (top panel). The stacked RFs of the selected stations are shown in the central plots, from station CCX to PIX, from top to bottom, in a west to east direction. The legend at the top-right of each stacked receiver function plot indicates the number of earthquakes used, the network code (BC), the station code, and the component code (HHQ). The dashed black line indicates the interpreted Ps arrivals. The right panel is a double plot that shows, for example, the back-azimuth coverage (black dots), and the distance of the earthquakes from the central point of the array (grey dots). The left panel is a plot of the altitude of the corresponding selected stations.

Figure 4. (a) Map of estimated depths from the *H-κ* analysis at each seismic station. Black thick lines indicate the analyzed profiles. The thin dotted line indicates the MGE. Plots (b), (c), and (d) show the back-projected RFs of the profiles A1-A1', A2-A2', and A3-A3', respectively; the

dashed green line indicates the suggested Moho from the interpreted ray paths. The figure from bellow of (b), (c), and (d) of the A1-A1', A2-A2', and A2-A2', respectively, shows: the results of Moho depth estimation with error bars from the *H*-κ procedure (Table 3); the elevation of the center of each profile, black line; mean sea level, thin black line; location of each station alongside the profile, black triangles; the location at which the A3-A3' crosses the profile, dashed line; the location at which A1-A1' and A2-A2' cross the profile, dotted lines.

Figure 5. Unified Moho model for northern Baja California. Each figure's upper plot is the local altimetry, and the color dots indicate the stations used for each study (right-handed legend box). The lower plots of (a) and (b) are the triangulation-based natural neighbor interpolation Moho estimations by seismic studies in northern Baja California; color dots represent the Moho estimations of each regional studies indicated in the right-handed legend box. Left and lower handed color bars indicate Moho depth and elevation (both in km), respectively. (a) Elevations and Moho estimations of northern Baja California from an S-N view. (b) Elevations and Moho estimations in northern Baja California from an NW-SE perspective.

663 **Figures**

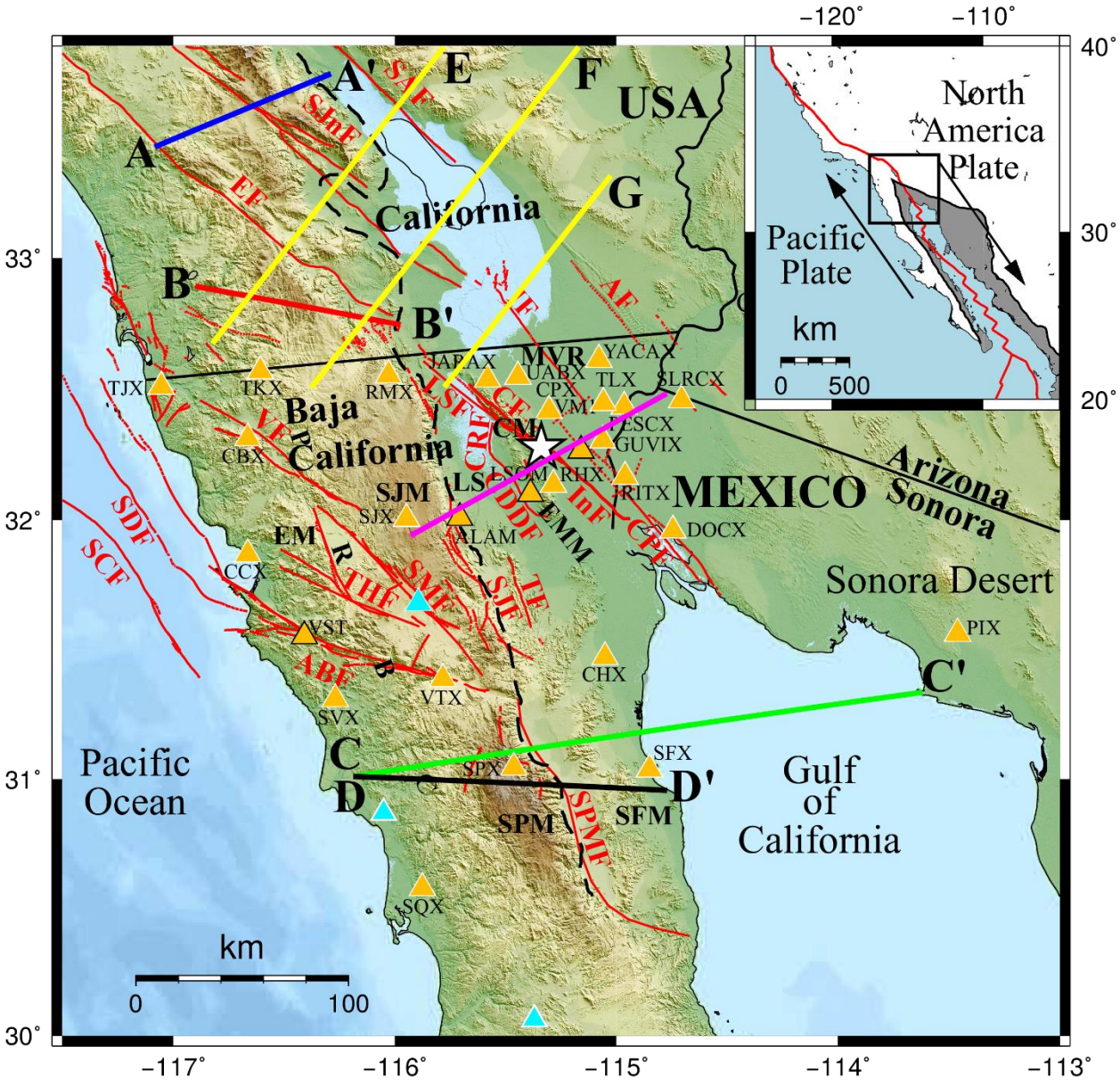

664

665

666 **Figure 2.**

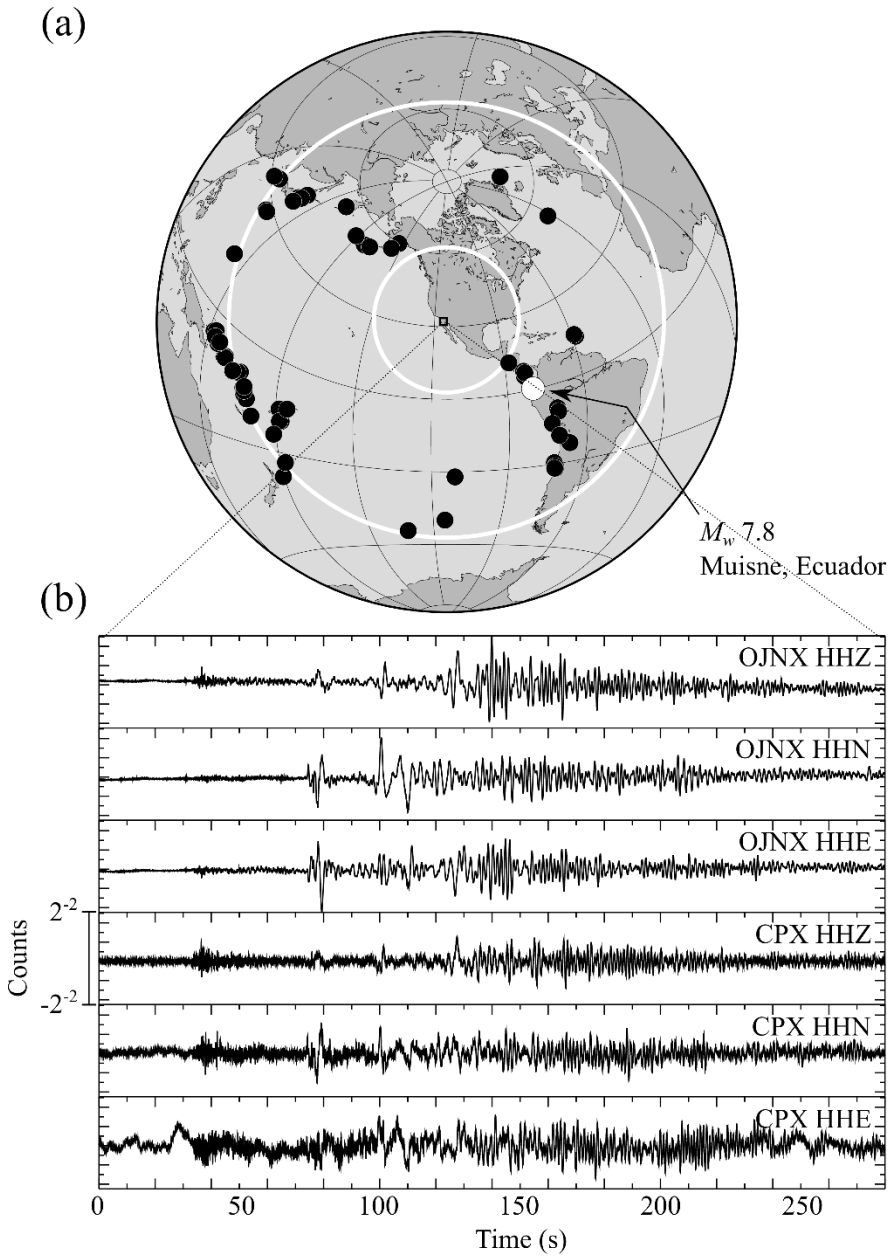

667

668

669

670 **Figure 3.**

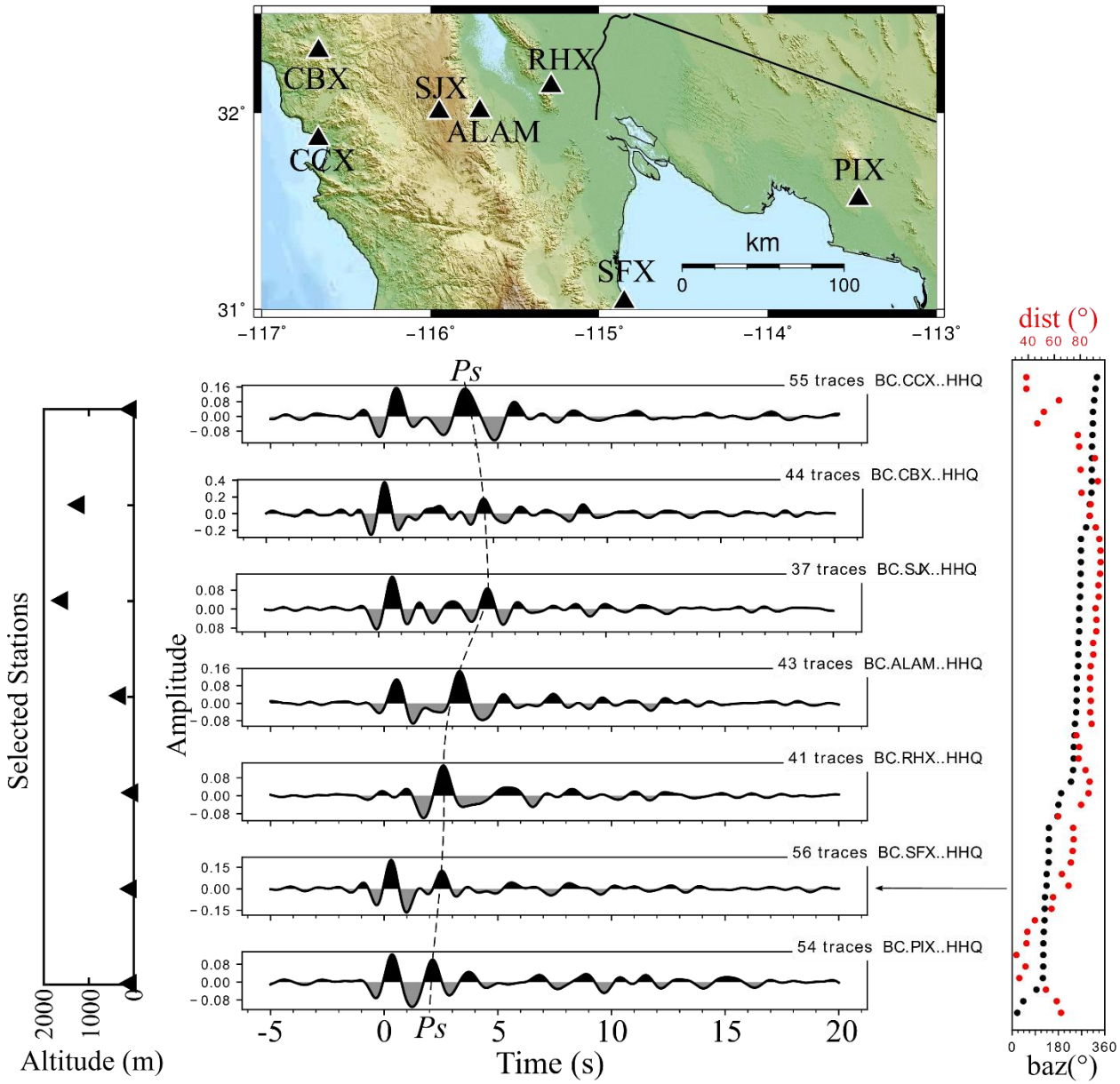

Figure 4.

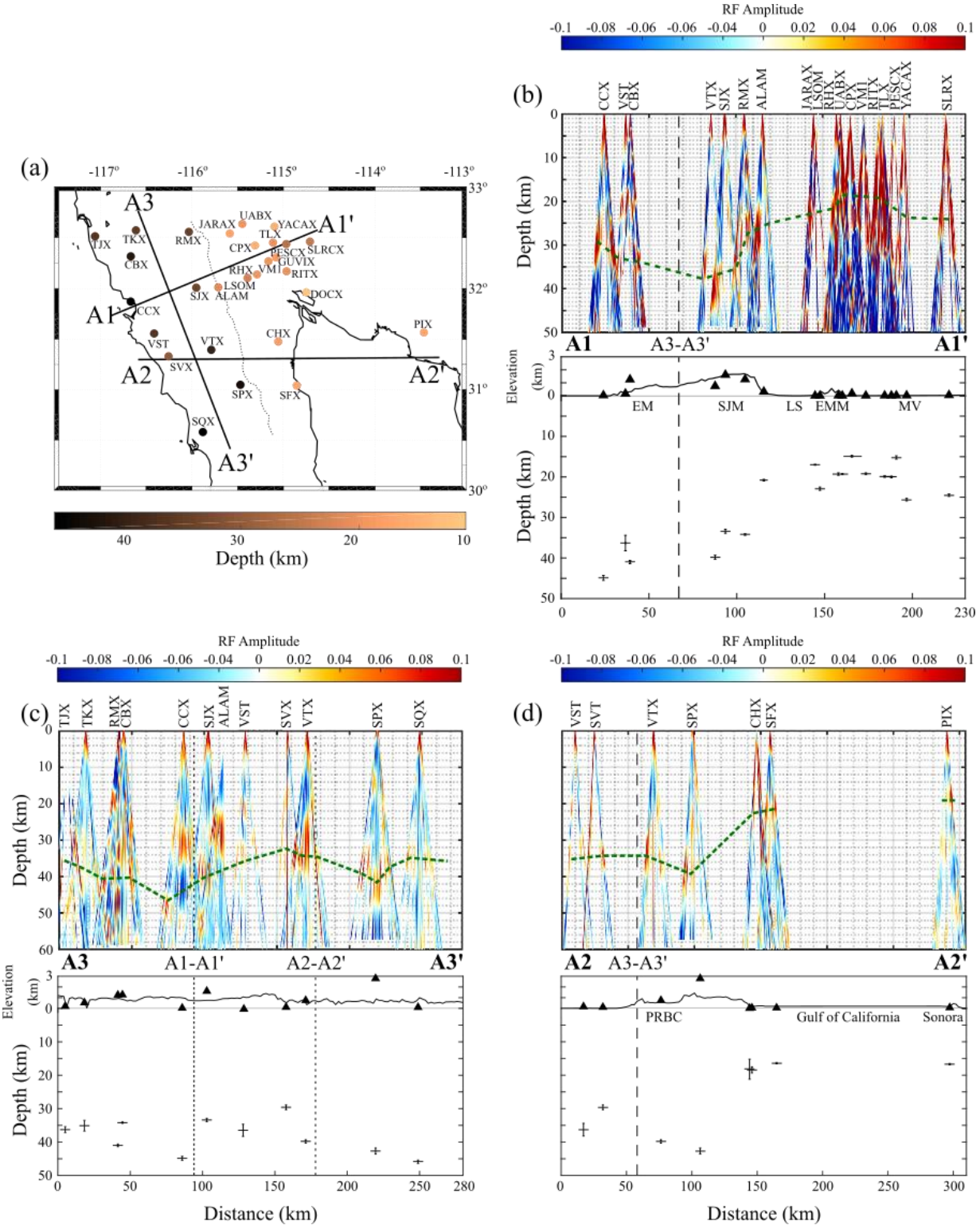

Figure 5.

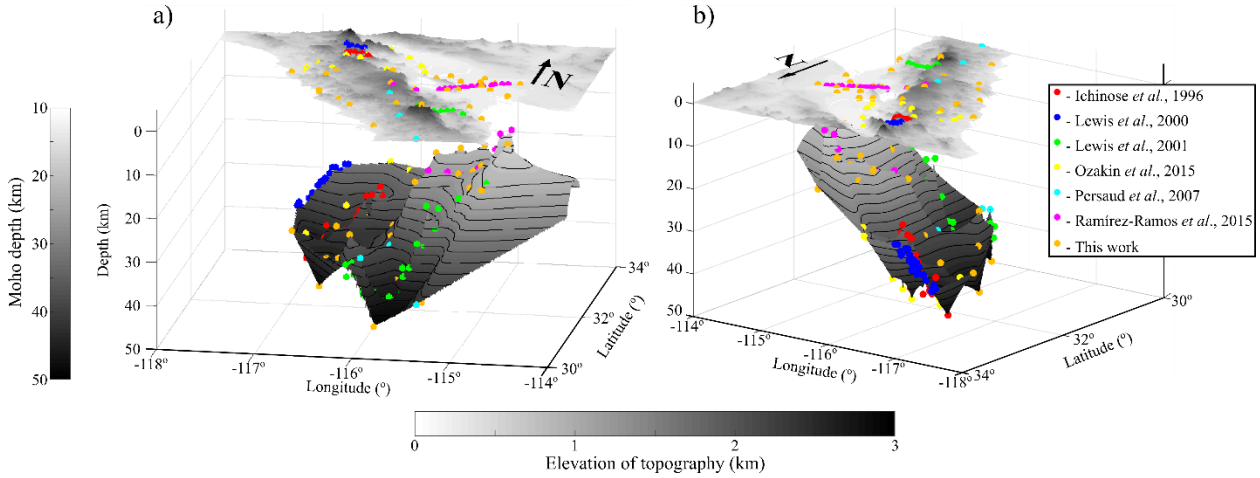

677

678

679 **Table 1.**

680 Permanent (RESNOM) and temporary broadband stations in northern Baja California.

Station Code	Sensor	Latitude (º)	Longitude (º)
ALAM[a,b]	NTC-120s	32.0085	-115.7074
CBX	CMG-40T	32.3131	-116.6636
CCX	CMG-3ESPC	31.8678	–116.6645
CHX	CMG-40T / CMG-3ESPC	31.4721	–115.0521
CPX	CMG-3ESPC	32.4195	–115.3050
DOCX	NTC-120s	31.9594	–114.7451
GUVIX	NTC-120s	32.3029	–115.0762
JARAX	NTC-120s	32.5378	–115.5815
LSOM[a]	NTC-120s	32.1000	-115.3878
PESCX	NTC-120s	32.4338	–114.9649
PIX	CMG-3ESPC	31.5629	–113.4599
RHX	CMG-3ESPC / NTC-120s	32.135	–115.2843
RITX	NTC-120s	32.1659	–114.9613
RMX	CMG-3ESPC / NTC-120s	32.5535	–116.0290
SFX	CMG-3ESPC	31.0376	–114.8510
SJX	CMG-3ESPC	32.0048	–115.9480

SLRCX	NTC-120s	32.4579	–114.7058
SPX	CMG-3ESPC	31.0451	–115.4660
SQX	CMG-3ESPC	30.5762	–115.8758
SVX	NTC-120s	31.3271	-116.2510
TJX	CMG-3ESPC / NTC-120s	32.5102	–117.0543
TKX	CMG-3ESPC / NTC-120s	32.5687	–116.6075
TLX	CMG-40TD	32.448	-115.109
UABX	CMG-3ESPC / NTC-120s	32.6316	-115.4447
VM1[a,b]	NTC-120s	32.2653	-115.1596
VST[a]	NTC-120s	31.5528	-116.4085
VTX	CMG-3ESPC	31.3914	-115.7840
YACAX	NTC-120s	32.6054	-115.0938

[a]Temporary broadband station.

[b]Temporary broadband station that later became a permanent seismic station of the RESNOM.

Table 2.

Earthquakes used for the receiver function analysis[a,b].

Date	Origin Time (HH:MM:SS)	Latitude (°)	Longitude (°)	Depth (km)	Magnitude (M_w)	Distance (°)	Azimuth (°)	Back-Azimuth (°)
28 April 2016	19:33:24.07	-16.0429	167.3786	24.00	7.0	87.94	236.82	56.82
16 April 2016	23:58:36.98	0.3819	-79.9218	20.59	7.8	46.35	133.32	313.32
15 April 2016	16:25:06.22	32.7906	130.7543	10.00	7.0	89.77	270.34	90.34
03 April 2016	08:23:52.32	-14.3235	166.8551	26.00	6.9	87.39	237.94	57.94
30 January 2016	03:25:12.22	53.9776	158.5463	177.00	7.2	62.12	289.45	109.45
24 January 2016	10:30:30.23	59.6363	-153.4051	129.00	7.1	37.04	317.12	137.12
14 January 2016	03:25:33.64	41.9723	142.7810	46.00	6.7	76.68	276.88	96.88
26 November 2015	05:45:18.40	-9.1825	-71.2574	602.75	6.7	59.22	134.28	314.28
24 November 2015	22:45:38.88	-10.5372	-70.9437	606.21	7.6	60.42	134.98	314.98
18 November 2015	18:31:04.57	-8.8994	158.4217	12.59	6.8	91.33	243.41	63.41
13 November 2015	20:51:31.03	31.0009	128.8729	12.00	6.7	92.14	269.29	89.29
11 November 2015	02:46:19.83	-29.5097	-72.0585	10.00	6.9	74.30	146.14	326.14
09 November 2015	16:03:46.07	51.6394	-173.0746	15.00	6.5	45.51	294.72	114.72
07 November 2015	07:31:43.87	-30.8796	-71.4519	46.00	6.8	75.71	146.42	326.42

20 October 2015	21:52:02.56	-14.8595	167.3028	135.00	7.1	87.33	237.49	57.49
21 September 2015	17:40:00.06	-31.7275	-71.3792	35.00	6.6	76.42	146.76	326.76
16 September 2015	22:54:32.86	-31.5729	-71.6744	22.44	8.3	76.14	146.87	326.87
12 August 2015	18:49:24.08	-9.3293	157.8772	6.43	6.5	92.01	243.33	63.33
10 August 2015	04:12:15.81	-9.3438	158.0525	22.00	6.6	91.87	243.27	63.27
27 July 2015	04:49:46.40	52.3760	-169.4458	29.00	6.9	43.33	297.18	117.18
18 July 2015	02:27:33.82	-10.4012	165.1409	11.00	7.0	86.59	240.66	60.66
16 July 2015	15:16:33.78	13.8672	-58.5479	20.00	6.5	54.98	109.36	289.36
10 July 2015	04:12:42.54	-9.3070	158.4030	12.00	6.7	91.56	243.20	63.20
3 June 2015	12:18:30.27	27.7375	139.7254	460.00	6.5	86.61	267.17	87.17
30 June 2015	11:23:02.11	27.8386	140.4931	664.00	7.8	86.00	267.21	87.21
29 June 2015	07:00:09.00	56.5940	-156.4300	72.60	6.7	37.08	310.56	130.56
22 June 2015	21:45:19.48	-11.0559	163.6959	11.19	6.9	88.13	240.74	60.74
20 June 2015	22:48:53.42	-10.8759	164.1694	11.00	6.8	87.65	240.69	60.69
19 June 2015	15:25:21.08	-54.3312	-132.1618	7.20	6.7	87.72	189.47	9.47
12 June 2015	21:12:58.89	38.9056	142.0317	35.00	6.8	78.79	274.60	94.60
07 June 2015	07:10:19.59	-7.2175	154.5567	10.00	7.1	93.67	245.30	65.30
05 June 2015	01:44:06.38	-5.4624	151.8751	55.00	7.5	95.00	246.85	66.85
01 June 2015	08:06:03.48	-5.2005	151.7773	44.00	6.8	94.94	247.01	67.01
17 June 2015	15:52:51.48	-15.8815	-178.6005	10.00	6.5	77.05	231.45	51.45
29 March 2015	23:48:31.01	-4.7294	152.5623	41.00	7.5	94.03	247.08	67.08
16 February 2015	23:06:28.27	39.8558	142.8808	23.00	6.7	77.73	275.32	95.32
13 February 2015	18:59:12.23	52.6487	-31.9016	16.68	7.1	61.33	71.47	251.47
11 February 2015	18:57:22.46	-23.1125	-66.6880	223.00	6.7	72.45	139.75	319.75
23 January 2015	03:47:27.05	-17.0309	168.5200	219.96	6.8	87.60	235.89	55.89
07 January 2015	05:07:07.51	5.9045	-82.6576	8.00	6.5	40.48	130.48	310.48
08 December 2014	08:54:52.52	7.9401	-82.6865	20.00	6.6	39.04	128.38	308.38
07 December 2014	01:22:02.18	-6.5108	154.4603	23.00	6.6	93.37	245.70	65.70
16 November 2014	22:33:20.45	-37.6478	179.6621	22.00	6.7	92.25	220.87	40.87
01 November 2014	18:57:22.38	-19.6903	-177.7587	434.00	7.1	78.88	228.91	48.91
14 October 2014	03:51:34.46	12.5262	-88.1225	40.00	7.3	32.00	127.92	307.92
09 October 2014	02:14:31.44	-32.1082	-110.8112	16.54	7.0	64.49	175.93	355.93
17 September 2014	06:14:45.41	13.7641	144.4294	130.00	6.7	90.84	258.59	78.59
20 August 2014	23:21:45.52	-14.5980	-73.5714	101.00	6.8	61.75	139.25	319.25
21 July 2014	14:54:41.00	-19.8015	-178.4001	615.42	6.9	79.41	229.14	49.14
11 July 2014	19:22:00.82	37.0052	142.4525	20.00	6.5	79.53	273.27	93.27
04 July 2014	15:00:27.86	-6.2304	152.8075	20.00	6.5	94.62	246.23	66.23
29 June 2014	17:15:09.34	-14.9831	-175.5096	18.00	6.7	74.19	230.57	50.57
23 June 2014	20:53:09.70	51.8486	178.7352	109.00	7.9	50.58	292.20	112.20
13 May 2014	06:35:24.24	7.2096	-82.3045	10.00	6.5	39.82	128.83	308.83

12 May 2014	18:38:36.70	-49.9403	-114.7995	10.47	6.5	82.17	179.47	359.47
04 May 2014	09:15:52.88	-24.6108	179.0856	527.00	6.6	84.28	227.66	47.66
01 May 2014	06:36:35.55	-21.4542	170.3546	106.00	6.6	88.74	232.86	52.86
13 April 2014	12:36:19.23	-11.4633	162.0511	39.00	7.4	89.71	241.01	61.01
12 April 2014	20:14:39.30	-11.2701	162.1481	22.56	7.6	89.52	241.08	61.08
11 April 2014	07:07:23.13	-6.5858	155.0485	60.53	7.1	92.92	245.51	65.51
01 April 2014	23:46:47.26	-19.6097	-70.7691	25.00	8.2	67.31	140.31	320.31
18 February 2014	09:27:13.12	14.6682	-58.9272	14.83	6.5	54.26	108.74	288.74
07 February 2014	08:40:13.55	-15.0691	167.3721	122.00	6.5	87.40	237.35	57.35
02 February 2014	09:26:37.82	-32.9076	-177.8806	44.26	6.5	87.64	222.07	42.07
01 January 2014	16:03:29.00	-13.8633	167.2490	187.00	6.5	86.81	238.06	58.06
30 August 2012	13:43:25.17	71.4410	-10.6050	14.00	6.8	64.18	56.42	236.42

[a]Origin time, location and magnitude provided by USGS (see Data and Resources).

[b] Distance, Azimuth and Back-Azimuth, resulted from Matlab-based scripts, with computations relative to the central point of the array: 32.1º N, 115.7º W.

Table 3.

Receiver function results and Moho estimations of each station.

Station code	Elevation (m)	*Ps-P* time (s)	*H* (km)	V_P/V_S, κ	Poisson's Ratio
ALAM	315	3.2	20.8 ± 0.2	1.84 ± 0.02	0.292 ± 0.005
CBX	1250	4.5	41.0 ± 0.4	1.96 ± 0.01	0.324 ± 0.004
CCX	33	3.6	44.9 ± 0.6	1.97 ± 0.02	0.327 ± 0.004
CHX	49	2.5	18.4 ± 0.9	1.74 ± 0.06	0.252 ± 0.024
CPX	179	3.2	14.9 ± 0.2	1.95 ± 0.02	0.321 ± 0.005
DOCX	13	1.4	10.9 ± 0.2	1.95 ± 0.03	0.208 ± 0.015
GUVIX	14	3.3	18.2 ± 3.0	1.87 ± 0.10	0.299 ± 0.026
JARAX	5	2.5	17.0 ± 0.1	1.85 ± 0.01	0.292 ± 0.004
LSOM	5		22.9 ± 0.4	1.55 ± 0.02	0.140 ± 0.012
PESCX	23	1.8	25.6 ± 0.3	1.72 ± 0.01	0.246 ± 0.005
PIX	72	2.2	16.7 ± 0.2	1.81 ± 0.02	0.280 ± 0.005
RHX	16	2.5	19.3 ± 0.3	1.75 ± 0.02	0.260 ± 0.008

RITX	14	1.8	20.0 ± 0.2	1.54 ± 0.01	0.137 ± 0.008
RMX	1265	4.7	34.2 ± 0.2	1.61 ± 0.01	0.186 ± 0.005
SFX	48	2.6	16.4 ± 0.2	1.97 ± 0.02	0.327 ± 0.004
SJX	1609	4.8	33.4 ± 0.5	1.57 ± 0.01	0.158 ± 0.008
SLRCX	49	1.2	24.5 ± 0.3	1.75 ± 0.02	0.256 ± 0.008
SPX	2790	4.9	42.7 ± 0.9	2.04 ± 0.03	0.341 ± 0.006
SQX	101	3.4	45.9 ± 0.5	1.96 ± 0.01	0.323 ± 0.003
SVX	111	4.1	29.6 ± 0.7	1.82 ± 0.03	0.282 ± 0.010
TJX	198	3.9	36.3 ± 0.9	1.62 ± 0.02	0.194 ± 0.012
TKX	535	3.3	35.1 ± 1.6	1.90 ± 0.04	0.309 ± 0.011
TLX	17	2.0	19.9 ± 0.2	1.95 ± 0.02	0.321 ± 0.004
UABX	5	3.5	19.3 ± 0.1	1.49 ± 0.01	0.090 ± 0.001
VM1	10	2.2	19.2 ± 0.2	1.64 ± 0.02	0.204 ± 0.009
VST	163	3.7	36.3 ± 1.9	1.65 ± 0.04	0.209 ± 0.0.21
VTX	746	4.1	39.8 ± 0.5	1.92 ± 0.02	0.315 ± 0.005
YACAX	21	1.9	15.2 ± 0.4	2.06 ± 0.04	0.346 ± 0.008

691

692